

CZECH TECHNICAL UNIVERSITY IN PRAGUE
FACULTY OF NUCLEAR SCIENCES AND PHYSICAL ENGINEERING
DEPARTMENT OF PHYSICS

Programme: Applied natural sciences
Branch of Study: Physics and Technology of Nuclear Fusion



Heat Transfer Analysis of ITER First Wall Panels

Analýza přestupu tepla panely první stěny reaktoru ITER

MASTER'S THESIS

Author: Bc. Ján Uličný
Supervisor: Phani Kumar Domalapally, Ph.D.
Consultant: Ing. Slavomír Entler
Submitted in: January 2016

VLOZENI ZADANI PRACE S PODPISEM DEKANA

Prohlášení

Prohlašuji, že jsem svou bakalářskou práci vypracoval samostatně a použila jsem pouze podklady (literaturu, projekty, SW atd.) uvedené v příloženém seznamu.

Nemám závažný důvod proti použití tohoto školního díla ve smyslu § 60 Zákona č. 121/2000 Sb., o právu autorském, o právech souvisejících s právem autorským a o změně některých zákonů (autorský zákon).

V Praze dne

.....

Bc. Ján Uličný

Název práce:

Analýza přestupu tepla panely první stěny reaktoru ITER

Autor: Bc. Ján Uličný

Obor: Fyzikální inženýrství

Druh práce: Diplomová práce

Vedoucí práce: Phani Kumar Domalapally, Ph.D.
Centrum výzkumu Řež

Konzultant: Ing. Slavomír Entler
Centrum výzkumu Řež

Abstrakt: Tato práce se zabývá přestupem tepla panely první stěny reaktoru ITER. Nej dříve je stručně zmíněna teorie přestupu tepla. Hlavní část práce se věnuje vytvoření modelu chladicího systému panelů a analýze vlivu tepelného toku a průtoku chladicí vody prostřednictvím parametrického výpočtu. V závěru jsou výsledky diskutovány.

Klíčová slova: přestup tepla, první stěna, ITER, HELCZA

Title:

Heat Transfer Analysis of ITER First Wall Panels

Author: Bc. Ján Uličný

Abstract: This thesis is concerned with analyzing the heat transfer in ITER first wall panels. First, brief introduction into theory of heat transfer is provided. The main part of the thesis looks into the development of a model of the cooling system of the panels and into the parametric sweep over heat flux and mass flow rate. In the last section, the results are discussed.

Key words: heat transfer, first wall, ITER, HELCZA

Contents

| | | |
|----------|--|-----------|
| 1 | Introduction | 1 |
| 1.1 | Thermonuclear fusion | 1 |
| 1.2 | ITER blanket and first wall | 3 |
| 1.3 | HELCA | 7 |
| 1.4 | Thesis objective | 10 |
| 2 | Heat transfer | 11 |
| 2.1 | Basic concepts | 11 |
| 2.1.1 | Mechanisms of heat transfer | 12 |
| 2.2 | Conjugate heat transfer | 12 |
| 2.3 | Conduction in solids | 13 |
| 2.3.1 | Boundary conditions | 13 |
| 2.3.2 | One-dimensional steady-state conduction | 15 |
| 2.4 | Estimating heat transfer coefficient | 16 |
| 2.4.1 | Internal forced convection with turbulent flow | 17 |
| 2.4.2 | Flow boiling | 19 |
| 3 | Heat transfer analysis of ITER FW06A panel | 23 |
| 3.1 | Description | 23 |
| 3.1.1 | Materials | 25 |
| 3.1.2 | Simplifications | 27 |
| 3.2 | General thermal analysis | 28 |
| 3.2.1 | Convective heat transfer coefficient | 29 |
| 3.3 | 1D model | 33 |
| 3.4 | 2D model | 38 |
| 3.5 | 3D model | 38 |
| 4 | Results | 45 |
| 4.1 | 1D model | 45 |
| 4.2 | 2D model | 47 |
| | Discussion | 53 |
| 4.3 | Conclusion | 54 |
| A | | 56 |

Chapter 1

Introduction

Thermonuclear fusion. Power of stars.

Since its discovery, fusion has provoked many minds with its enormous potential. Just imagine what one could do if he could control the energy source of the universe. And indeed, man has found a way in a form of thermonuclear bomb. Its effects were even more devastating and terrifying than those of an atomic bomb. Following the example set by atomic bomb and fission reactors, the use of fusion for electricity production seemed just a few years down the road. But taming the power of the Sun proved and proves to be much more challenging. With nuclear fission power plants in operation for over six decades, fusion power plants do not appear to be any closer to reality than in the atomic age. In fact, the most optimistic estimation expect first commercial power plant around year 2050. Still, the dream of fusion power is so intriguing and the payoff so great that fusion research will undoubtedly continue and hopefully, we will see the power of stars used for peaceful purposes on the Earth.

1.1 Thermonuclear fusion

Mass of every atom nucleus has mass larger than total mass of its constituent nucleons. The difference between these masses is proportional to the binding energy of the nucleus according to Einstein's famous equation:

$$E = c^2(Zm_p + (A - Z)m_n - m), \quad (1.1)$$

where E is binding energy, c is speed of light, Z is atomic number, A is atomic number, m_p is mass of proton, m_n is mass of neutron, and m is mass of nucleus.

Figure 1.1 shows binding energy per nucleon. Iron with its highest binding energy divides elements in to two categories:

1. Atoms to the left of iron are lighter than iron and if they form a larger nucleus, excessive binding energy is released. However, if such nucleus was to break up, some additional energy is required. This is domain of nuclear fusion.
2. Atoms to the right of iron can split into smaller ones with energy gain. This process is utilized in nuclear fission.

Generally, nuclear fusion is any nuclear reaction in which, several lighter nuclei fuse to a heavier one. These reactions conserve energy, but do not conserve mass. In a case of total

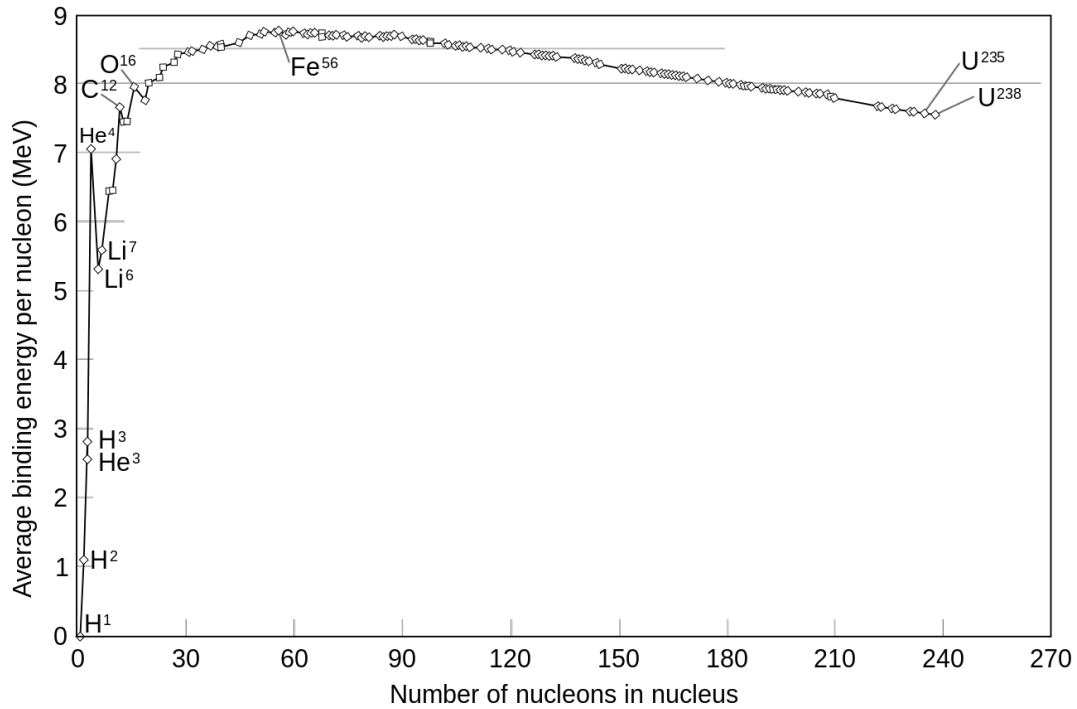


Figure 1.1: Binding energy per nucleon. [20]

mass of reactants being bigger than the sum of mass of products, this reaction has energy gain, which manifests itself as kinetic energy of products.

Unfortunately, repulsive Coulomb interaction makes it very difficult for nuclei to get close enough together that attractive strong interaction exceeds Coulomb forces and nuclei fuse. Many orders of magnitude higher cross section of Coulomb interaction compared to cross section of strong interaction makes it impossible to simply use particle accelerators to produce fusion energy, because dissipative energy losses in Coulomb collisions are much bigger than energy gain from fusion reactions. Yet, if the motion of particles is random, the Coulomb collisions just redistribute kinetic energy among particles and energy is not lost through this interaction. This is referred to as thermonuclear fusion.

To use thermonuclear fusion as energy source, there must be certain conditions met in the reactor. They were first formulated by J. D. Lawson [16], he calculated the requirements for energy surplus in the reactor and found out that there are three key quantities: temperature inside the reactor, density of fuel and confinement time. The temperature or in other words, the kinetic energy of particles, allows the overcoming of the Coulomb barrier. The density affects how many reactions will take place in an unit of volume and the confinement time tells us how quickly the reactor loses energy. By multiplication of these three quantities we obtain a new one called *triple product*, which is a useful benchmark for comparing different fusion reactors as it states the overall conditions needed for operating the reactor with self-sustainable fusion reaction.

How to achieve these conditions? The Sun relies on its enormous mass, gravitationally compressing its core to reach temperatures of about 150 million Kelvin. Obviously, this is not a solution applicable on Earth. Currently, there are two most promising ways: inertial and magnetic confinement.

Inertial confinement fusion *ICF* is basically a small, technologically manageable, thermonuclear explosion. The confinement mechanism is based on inertia, fusion reaction manages to burn substantial amount of fuel before it becomes too scattered. Usually, the initial fuel compression is performed by lasers. The biggest experiments include National Ignition Facility in Livermore, USA and French Laser Mégajoule.

Magnetic confinement fusion *MCF* traps the plasma with strong magnetic field. From countless magnetic configurations, tokamak is the most promising one. Tokamak is essentially a doughnut-shaped vacuum chamber surrounded by coils creating strong toroidal magnetic field, which holds plasma inside the vessel and prevents it from touching the chamber walls. There are dozens of tokamaks in operation around the world including tokamaks GOLEM and COMPASS in Czech republic. Presently, the largest tokamak is Joint European Torus *JET* in Culham in United Kingdom, but it will lose its record when International Thermonuclear Experimental Reactor *ITER* is built.

ITER is one of the most demanding, expensive, and ambitious science projects of all times, with scope similar to that of International Space Station or Large Hadron Collider in CERN. Its purpose is to our deepen understanding of plasma physics, explore material and technology possibilities for fusion reactors, test various support subsystems and ultimately, pave the way for a prototype fusion power plant DEMO.

European Union is a major player in the fusion research and its strategy for next decades is formulated in the document *Fusion Electricity – A roadmap to the realisation of fusion energy* [7]. The role of DEMO is to demonstrate economic feasibility of fusion power and convince private sector that it is a competitive energy source. There are many advantages linked to the fusion electricity production, Smith and Ward name a few in *The path to fusion power* [22]:

1. **Abundant fuel supply**

First generation of fusion power plants will burn deuterium and tritium. There is virtually unlimited amount of deuterium on Earth in seawater and tritium can be bred inside reactors from lithium, which can be mined or also extracted from seawater.

2. **Safety**

Total mass of fuel in reactor is very small at every moment and as a result, catastrophic runaway accident is impossible. In the worst case scenario of failed cooling system, radiation from activated materials would produce heat, but it would not affect structural integrity of the reactor.

3. **Low land use**

Size of a fusion power plant would be comparable to nuclear or fossil one.

4. **Clean energy**

In principle, fusion products from D-T reaction are not radioactive. However, there will be secondary radiation from materials activated by fusion neutrons. Albeit, if the materials are carefully selected, so their half-lives of decay are sufficiently low, the power plant could be fully recycled in 100 years after closing.

1.2 ITER blanket and first wall

ITER, shown in the figure 1.2, aims to produce 500 *MW* of fusion power with plasma heating input of roughly 50 *MW*. It is a technological challenge to exhaust this much heat and vital

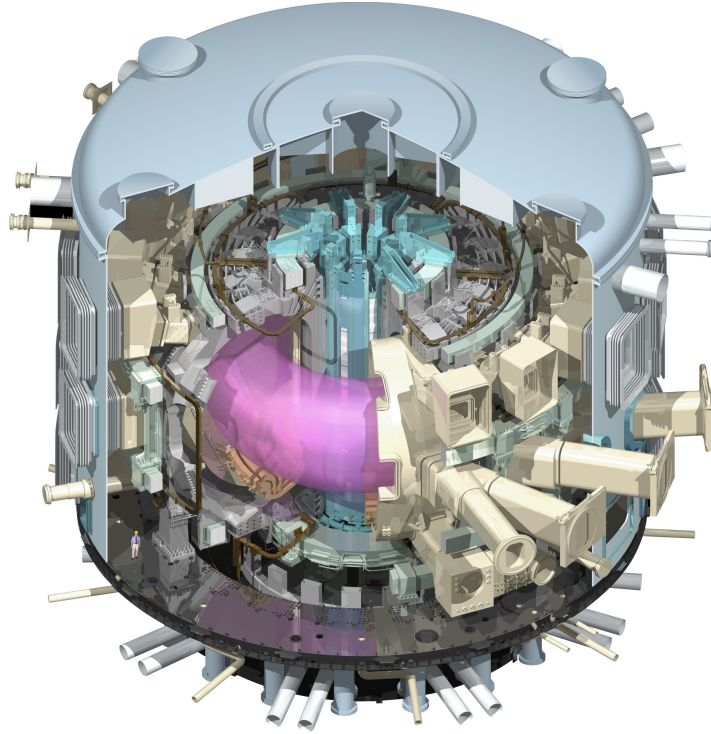


Figure 1.2: The ITER Tokamak [13]

role in it plays an essential component lining the vacuum vessel - the blanket system.

The blanket system has many functions [18], the main are to

- absorb particle and radiation heat fluxes from the plasma,
- provide thermal and neutron shielding of superconducting coils, vessel and external structures,
- provide suitable plasma facing surfaces to reduce influx of high-Z impurities to the plasma,
- serve as a limiting surface during startup and shutdown phases of operation.

The blanket system covers area of approximately 600 m^2 and consists of 440 blanket modules, segmented into 18 poloidal rows - 6 inboard, 4 upper and 8 outboard. The typical dimensions of blanket modules are about $(1\text{m} \times 1.4\text{m} \times 0.5 \text{ m})$ and all of them together weigh around 1530 tons. Fig. 1.3 illustrates position of these modules in the vessel. Each blanket module consists of a shield block and a first wall (FW) panel as seen in the fig. 1.4. The shield block provides structural support and neutron shielding, the FW panel thermal exhaust and plasma facing surface. [21]

Blanket modules are mechanically and electrically attached to the vessel, hydraulic connection is provided via blanket manifold - a system of pipes running behind or between shielding blocks. It is possible to replace blanket modules with remote handling. Lifetime of shield blocks is designed to be for ITER lifetime. However, the lifetime of the FW panels is 15,000 discharges, so they will need to be replaced at least once during ITER operation. For this

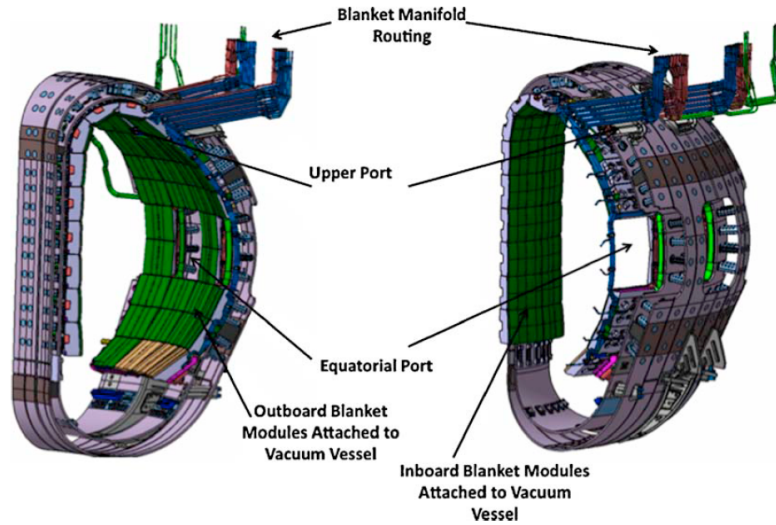


Figure 1.3: Blanket modules in inboard and outboard regions. [21]

reason, the FW panels are connected to the shield block with a central bolt, enabling quick replacement in case they are damaged.

Structure of FW panel is apparent from fig. 1.5. The FW panels have their own supporting structure - a poloidally oriented I-beam made from stainless steel providing support and hydraulic connection to plasma facing units, which are attached to it. Each plasma facing unit consists of several dozens of fingers, so electromagnetic loads caused by eddy currents are reduced. The fingers use beryllium tiles as low-Z plasma facing material, copper as a compliance layer and diffusion barrier, copper-chromium-zirconium alloy as heat sink and into the heat sink layer are embedded stainless steel tubes for coolant.

The FW panels are cooled by water with inlet temperature $70\text{ }^{\circ}\text{C}$ and outlet temperature $110\text{ }^{\circ}\text{C}$ pressurized to 3 MPa . Standard pressure drop of the hydraulic circuit is 0.1 MPa at 3 MPa and $100\text{ }^{\circ}\text{C}$.

To avoid local overheating due to individual panels misalignment, plasma facing surface is shaped. This shaping and FW panel dimensions depend on the position of the panel in the vessel. Currently, more than 100 different designs of panels exist. This number is expected to be reduced to about 30 final types of FW panels for ITER.

In the flat top stage of an experiment, the heat load on the first wall panels will be 550 MW , and the heat flux distribution will not be homogeneous. On top of that, during startup and shutdown, the heat flux on limiting surfaces will be even greater than in the flat top phase. Consequently, this demands two types of first wall fingers [21]:

EHF - enhanced heat flux panels capable of handling heat fluxes up to $5\text{ MW}/\text{m}^2$ will be used in limiting surfaces in the outboard and inboard region and at the top of chamber near secondary X-point. The rectangular cooling channel is equipped with hypervapotron to enhance heat transfer.

NHF - normal heat flux panels for fluxes of $1 - 2\text{ MW}/\text{m}^2$ are to be used elsewhere.

This design uses stainless steel cooling tubes embedded in CuCrZr alloy.

They are further separated to:

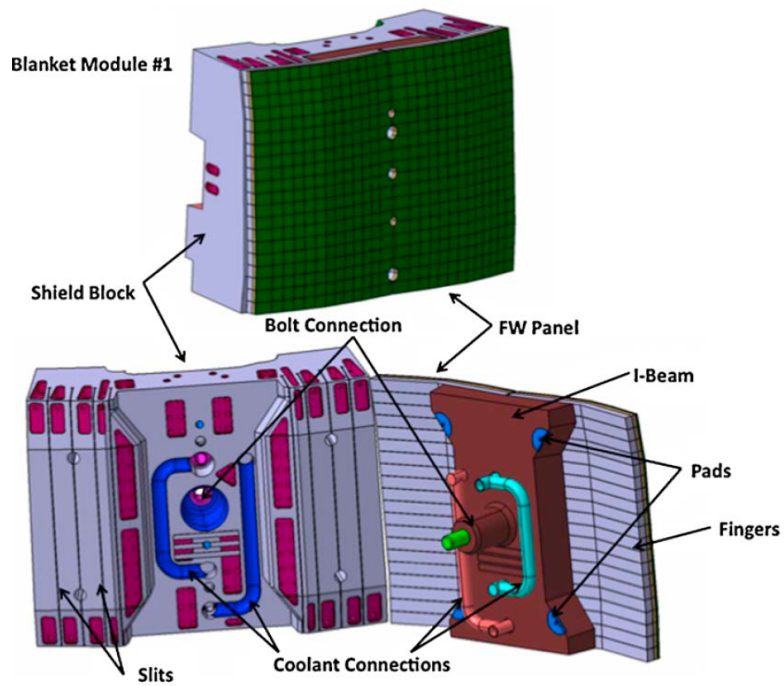


Figure 1.4: Typical blanket module consisting of the shield block and the first wall panel. [21]

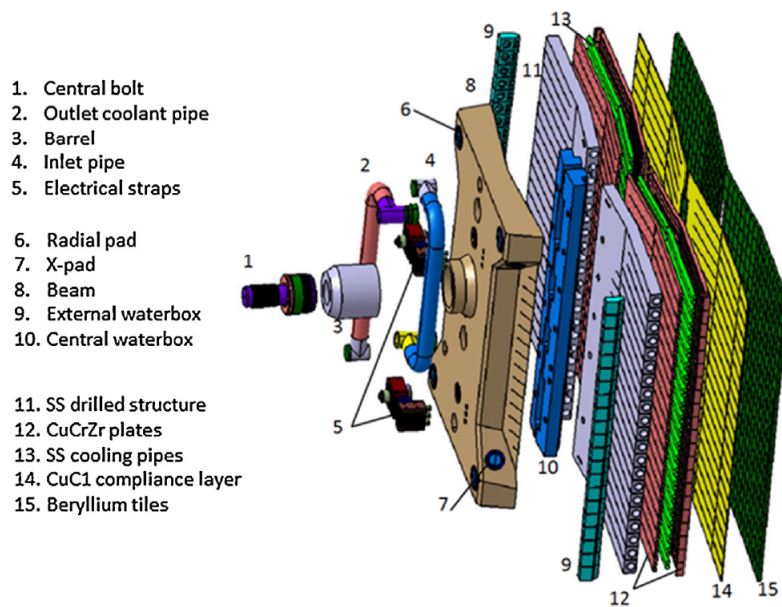


Figure 1.5: Typical NHF FW panel in exploded view. [4]

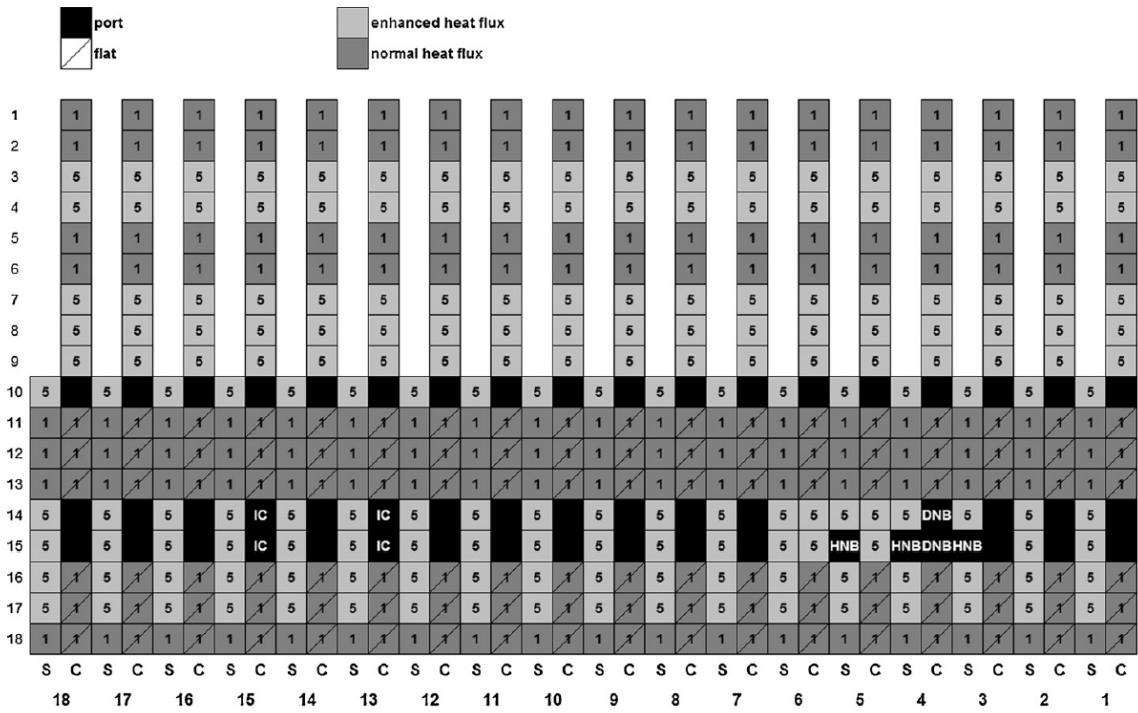


Figure 1.8: Distribution map of normal and enhanced heat flux panels. Light gray - EHF, dark gray - NHF, black - ports. [19]

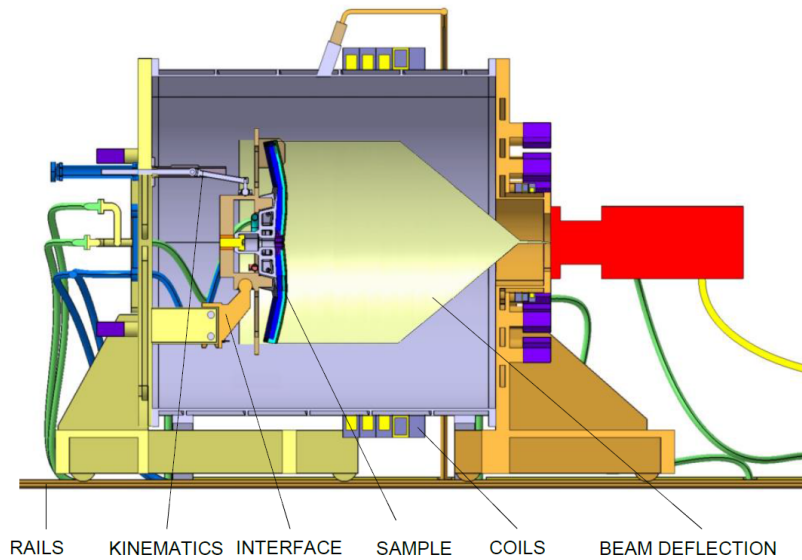


Figure 1.9: Schematics of HELCZA device. [8]

| Cycle label | Heating time [s] | Delay time [s] |
|---------------|------------------|----------------|
| Cycle 50/70 | 50 | 70 |
| Cycle 100/150 | 100 | 150 |
| Cycle 30/30 | 30 | 30 |

Table 1.1: Types of heat load cycles for FW testing in HELCZA.

| | Specification | Heat flux [MW/m^2] | Cycle type (see tab. 1.1) |
|----|-----------------|------------------------|--|
| 1. | Thermal mapping | 0.5 | until sample temperature stabilization |
| 2. | 11,900 cycles | 2.0 | cycle 50/70 |
| 3. | 100 cycles | 2.0 | cycle 100/150 |
| 4. | Thermal mapping | 0.5 | until sample temperature stabilization |
| 5. | 2,400 cycles | 2.5 | cycle 50/70 |
| 6. | 100 cycles | 2.5 | cycle 100/150 |
| 7. | Thermal mapping | 0.5 | until sample temperature stabilization |

Table 1.2: Test sequence for FW prototype panel testing in HELCZA.

| | Specification | Heat flux [MW/m^2] | Cycle type (see tab. 1.1) |
|----|-----------------|------------------------|--|
| 1. | Thermal mapping | 0.5 | until sample temperature stabilization |
| 2. | 1,000 cycles | 2.0 | cycle 50/70 |
| 3. | Thermal mapping | 0.5 | until sample temperature stabilization |
| 4. | 250 cycles | 2.5 | cycle 50/70 |
| 5. | Thermal mapping | 0.5 | until sample temperature stabilization |

Table 1.3: Test sequence for FW pre-series panel testing in HELCZA.

| | Specification | Heat flux [MW/m^2] | Cycle type (see tab. 1.1) |
|----|-----------------|------------------------|--|
| 1. | Thermal mapping | 0.5 | until sample temperature stabilization |
| 2. | 100 cycles | 2.0 | cycle 30/30 |
| 3. | Thermal mapping | 0.5 | until sample temperature stabilization |

Table 1.4: Test sequence for FW series panel testing in HELCZA.

1.4 Thesis objective

European domestic agency *Fusion for Energy* has set limits to ensure machine safety during the FW panels testing at HELCZA facility. These limits are:

- Cooling water outlet temperature T_e must be below $110\text{ }^\circ\text{C}$
- Maximum beryllium temperature T_{Be} can not exceed $500\text{ }^\circ\text{C}$

In HELCZA, two major parameters will influence the temperature of samples - heat flux from electron beam and cooling water mass flow rate. My task is to investigate effects of these parameters and to find out for what combination of heat flux and cooling water mass flow rate the Fusion for Energy limits are satisfied and therefore safe operation secured.

Ranges of parameters are:

- Electron beam effective heat flux density \dot{q} range: $(0.5 - 4.7)\text{ MW/m}^2$.
- Cooling water mass flow rate through one panel \dot{m}_{total} range: $(1 - 15)\text{ kg/s}$.

Chapter 2

Heat transfer

2.1 Basic concepts

Heat transfer is a study of exchange of thermal energy from one system to another. It gives answer to how much heat is exchanged and also provides information about rate of heat exchange and the time of heating or cooling.

The laws of thermodynamics also apply to the heat transfer theory. The first law of thermodynamics, a version of conservation of energy principle, states that *the change in amount of energy contained within a system during a time interval is equal to the net amount of energy transferred across the system boundary during that time interval* [17].

Energy can be transferred by two means: heat transfer Q [J] and work W [J]. If a temperature difference is the driving force of energy transfer, then it is heat transfer, otherwise, it is work. Heat transfer rate \dot{Q} [$W = J/s$] is defined as amount of heat transferred per unit of time. Heat flux density \dot{q} [W/m^2], or heat flux for short, is heat transfer rate per unit of area.

Treating the transformation of other forms of energy to heat as heat generation, the energy balance can be expressed as heat balance.

$$Q_{in} - Q_{out} + E_{gen} = \Delta E_{thermal}, \quad (2.1)$$

where Q_{in} is heat received by the system, Q_{out} is heat rejected, E_{gen} is heat generation, and $\Delta E_{thermal}$ is total change in thermal energy of the system.

In rate form:

$$\dot{Q}_{in} - \dot{Q}_{out} + \dot{E}_{gen} = \frac{dE_{thermal}}{dt}, \quad (2.2)$$

where \dot{Q}_{in} is heat addition transfer rate, \dot{Q}_{out} is heat rejection transfer, \dot{E}_{gen} is heat generation rate, and $E_{thermal}$ is total thermal energy of the system.

In case of steady-state process with no heat generation, the rate balance (2.2) reduces to:

$$\dot{Q}_{in} = \dot{Q}_{out}. \quad (2.3)$$

The second law of thermodynamics, in the form of *Clausius statement* states that *it is impossible for any system to operate in such a way that the sole result would be an energy transfer by heat from a cooler to a hotter body* [17]. As a result, heat transfer can occur only from a warmer body to a colder one and it stops once the temperature difference is equalized.

2.1.1 Mechanisms of heat transfer

Conduction

Transfer of kinetic energy through interaction between more energetic particles and adjacent less energetic ones. Conduction can occur in solids, liquids and gases. In solids, due to vibration of molecules and free electrons. And in fluids, due to the random motion of particles resulting in collisions and diffusion.

Conduction heat flux \dot{q}_{cond} obeys *Fourier's law of heat conduction*:

$$\dot{\mathbf{q}}_{\text{cond}} = -k\nabla T, \quad (2.4)$$

where k is thermal conductivity, and T is temperature.

Convection

Convection is heat transfer mode associated with combined conduction and bulk fluid motion. Convection occurs in liquids, gases, and in plasma.

Convection heat flux \dot{q}_{conv} obeys *Newton's law of cooling*:

$$\dot{\mathbf{q}}_{\text{conv}} = h(T_{\mathbf{s}} - T_{\infty}), \quad (2.5)$$

where h is convective heat transfer coefficient, $T_{\mathbf{s}}$ is surface temperature, and T_{∞} is fluid temperature far from surface.

Radiation

Radiation is a process of emitting energy in form of electromagnetic waves. It is the only mechanism that does not require a presence of medium and functions even in vacuum.

From *Stefan-Boltzmann law* for black-body radiation, we can derive equation for radiation heat flux \dot{q}_{rad} :

$$\dot{\mathbf{q}}_{\text{rad}} = \epsilon\sigma(T_{\mathbf{s}}^4 - T_{\text{amb}}^4), \quad (2.6)$$

where ϵ is emissivity, $\sigma = 5,6704 \cdot 10^{-8} \text{Wm}^{-2}\text{K}^{-4}$ is Stefan-Boltzmann constant, $T_{\mathbf{s}}$ is surface temperature, and T_{amb} is ambient temperature.

2.2 Conjugate heat transfer

Conjugate heat transfer refers to coupled heat transfer in solid body and in fluid that flows around it or inside it. ITER FW fingers are cooled by water flowing inside them and so the heat transfer is conjugate. The conjugate heat transfer is defined by set of equations for heat transfer in the solid, set of equations for heat transfer and movement in the fluid domain, conjugate conditions at the solid-fluid interface and set of initial and boundary conditions.

Calculating the fluid movement can be quite demanding task. Hopefully, there is a simpler, widely used approach that is strictly not conjugate heat transfer, but rather, heat conduction in solid with convective boundary condition. All effects of fluid heat transfer are incorporated into one number defined at solid-fluid interface - *heat transfer coefficient*.

For calculating heat transfer coefficient, we use correlations - formulas valid for a specific type of flow under specific conditions. Particularly for turbulent flow, the theoretical calculations are so difficult that we mainly rely on correlations based on experimental studies. Since there are so many conditions that can have an effect on convection heat transfer, it is very

tricky to choose the right correlation for a particular problem as was shown by Fang, Shi and Zhou in [9]. They have compared multiple correlations with their experiment and have discovered that the best correlation still had mean absolute relative difference of 36 %. Under those circumstances, it is obvious that this method provides qualitative instead of quantitative answers to heat transfer analysis.

2.3 Conduction in solids

Heat conduction in a medium is generally three-dimensional and time dependent problem. If the temperature distribution in a medium does not vary in time, the heat conduction is called *steady* or *steady-state*, if it does, it is called *unsteady* or *transient*. If the heat conduction is not significant in any direction, we can reduce the dimensionality of the problem and get *one-dimensional* or *two-dimensional* heat conduction.

Heat conduction is described by the heat conduction equation:

$$\rho c \frac{\partial T}{\partial t} = \nabla \cdot (k \nabla T) + \dot{e}_{\text{gen}} \quad (2.7)$$

where ρ is density of the medium, c is specific heat capacity of the medium, T is temperature, t is time, k is thermal conductivity of the medium, and \dot{e}_{gen} is rate of heat generation.

If the thermal conductivity is temperature and space independent, the equation (2.7) can be rewritten using thermal diffusivity α :

$$\frac{\partial T}{\partial t} = \frac{1}{\alpha} \Delta T + \frac{k}{\alpha} \dot{e}_{\text{gen}}. \quad (2.8)$$

The thermal diffusivity α is defined as:

$$\alpha = \frac{k}{\rho c}. \quad (2.9)$$

In case of steady-state conduction without heat generation, equation (2.8) reduces to

$$\Delta T = 0. \quad (2.10)$$

2.3.1 Boundary conditions

Mathematical expressions describing thermal conditions on boundaries are known as *boundary conditions (BC)*. When dealing with heat transfer, most common are:

1. Specified temperature - Dirichlet type BC

$$T(\mathbf{x}_{\text{BC}}) = T_{\text{BC}}, \quad (2.11)$$

where $T(\mathbf{x}_{\text{BC}})$ is temperature at boundary point \mathbf{x}_{BC} and T_{BC} is specified temperature boundary condition.

Generally, T_{BC} can be dependent on time, but in case of steady heat conduction T_{BC} is constant.

2. Specified heat flux - Neumann type BC

$$-k\nabla_{\mathbf{n}}T(\mathbf{x}_{\text{BC}}) = \dot{\mathbf{q}}_{\text{BC}}, \quad (2.12)$$

where k is thermal conductivity, $\nabla_{\mathbf{n}}T$ is temperature gradient in direction normal to the boundary at boundary point \mathbf{x}_{BC} and $\dot{\mathbf{q}}_{\text{BC}}$ is specified heat flux boundary condition. Special case of heat flux BC is *insulated boundary*:

$$\nabla_{\mathbf{n}}T(\mathbf{x}_{\text{BC}}) = 0. \quad (2.13)$$

3. Convection - Robin type BC

This boundary condition describing heat transfer at solid-fluid interface is based on energy balance at that interface:

$$\dot{\mathbf{q}}_{\text{cond}}(\mathbf{x}_{\text{BC}}) = \dot{\mathbf{q}}_{\text{conv}}(\mathbf{x}_{\text{BC}}), \quad (2.14)$$

where $\dot{\mathbf{q}}_{\text{cond}}$ is conduction heat transfer in solid at boundary point \mathbf{x}_{BC} and $\dot{\mathbf{q}}_{\text{conv}}$ is convection heat transfer at boundary point \mathbf{x}_{BC}

Substituting to equation (2.14) from Fourier's law (2.4) and Newton's law of cooling (2.5):

$$-k\nabla_{\mathbf{n}}T(\mathbf{x}_{\text{BC}}) = h(T(\mathbf{x}_{\text{BC}}) - T_{\infty}), \quad (2.15)$$

where k is thermal conductivity, $\nabla_{\mathbf{n}}T$ is temperature gradient in direction normal to the boundary at the boundary point \mathbf{x}_{BC} , h is local convective heat transfer coefficient, T is temperature at the boundary point \mathbf{x}_{BC} and T_{∞} is bulk fluid temperature sufficiently far from the interface.

4. Radiation

Similarly to convection boundary condition, radiation boundary condition satisfies energy balance:

$$\dot{\mathbf{q}}_{\text{cond}}(\mathbf{x}_{\text{BC}}) = \dot{\mathbf{q}}_{\text{rad}}(\mathbf{x}_{\text{BC}}), \quad (2.16)$$

where $\dot{\mathbf{q}}_{\text{cond}}$ is conduction heat transfer in solid at boundary point \mathbf{x}_{BC} and $\dot{\mathbf{q}}_{\text{rad}}$ is radiation heat transfer at boundary point \mathbf{x}_{BC} .

Substituting to equation (2.14) from Fourier's law (2.4) and expression for radiation heat transfer (2.6):

$$-k\nabla_{\mathbf{n}}T(\mathbf{x}_{\text{BC}}) = \epsilon\sigma(T(\mathbf{x}_{\text{BC}})^4 - T_{\text{amb}}^4), \quad (2.17)$$

where k is thermal conductivity, $\nabla_{\mathbf{n}}T$ is temperature gradient in direction normal to the boundary at the boundary point \mathbf{x}_{BC} , ϵ is emissivity, σ is Stefan-Boltzmann constant, T is temperature at the boundary point \mathbf{x}_{BC} , and T_{amb} is ambient temperature.

In reality, boundary condition are often combination of several above mentioned types. However, surface energy balance must be satisfied at all times.

2.3.2 One-dimensional steady-state conduction

Given that conduction is one-dimensional, steady-state and without heat generation, the heat conduction equation (2.7) becomes:

$$\frac{\partial}{\partial x} \left(k \frac{\partial T}{\partial x} \right) = 0, \quad (2.18)$$

where T is temperature, x is space coordinate and k is thermal conductivity.

Integrating once:

$$k \frac{\partial T}{\partial x} = C, \quad (2.19)$$

where C is integration constant.

Comparison with *Fourier's law* (2.4) implies that the integration constant C is equivalent to negative of heat flux \dot{q} and so

$$\dot{q}_{\text{cond}} = -k \frac{\partial T}{\partial x}, \quad (2.20)$$

where \dot{q}_{cond} is conduction heat flux.

Integrating this equation another time with respect to x would yield temperature distribution. Since thermal conductivity might be temperature and space dependent, this integration is non-trivial. But assuming thermal conductivity constant with respect to x , it is possible to factor it in the space derivative and equation (2.20) transforms to

$$\dot{q}_{\text{cond}} = -\frac{\partial}{\partial x} (kT). \quad (2.21)$$

Integrating gives:

$$kT = \dot{q}_{\text{cond}}x + C. \quad (2.22)$$

Rearrange to express T and rename the integration constant:

$$T = \frac{\dot{q}_{\text{cond}}}{k}x + T_0, \quad (2.23)$$

where T_0 is offset temperature.

To determine values of \dot{q}_{cond} and T_0 two boundary conditions are needed.

Consider one-dimensional case of conduction across medium of length L , with temperatures T_1 at one boundary and T_2 at the other. Equation (2.23) can be rewritten as

$$T_2 = \frac{\dot{q}_{\text{cond}}}{k}L + T_1, \quad (2.24)$$

and rearranged to

$$\dot{q}_{\text{cond}} = k \frac{T_2 - T_1}{L}. \quad (2.25)$$

It is convenient to introduce the concept of *thermal resistance* R_{cond} [$\frac{m^2K}{W}$]. Defined as

$$R_{\text{cond}} = \frac{L}{k}, \quad (2.26)$$

where L is length and k is thermal conductivity.

Equation (2.25) then becomes

$$\dot{q}_{\text{cond}} = \frac{T_2 - T_1}{R_{\text{cond}}}. \quad (2.27)$$

Analogically, the *convection resistance* R_{conv} of surface can be defined as

$$R_{\text{conv}} = \frac{1}{h}, \quad (2.28)$$

where h is heat transfer coefficient.

Substituting to equation for convection boundary condition (2.15) then yields

$$\dot{q}_{\text{conv}} = \frac{T_s - T_\infty}{R_{\text{conv}}}, \quad (2.29)$$

where \dot{q}_{conv} is convection heat flux, T_s is surface temperature (temperature at the boundary), T_∞ is bulk fluid temperature sufficiently far from the interface.

Thermal resistances can be combined to form thermal resistance networks. In a manner similar to the electric resistance theory, even thermal resistance network can be summed up and expressed in one number - total thermal resistance R_{total} .

In one-dimensional case, the resistances can be combined only into series and total thermal resistance R_{total} can be calculated as

$$R_{\text{total}} = \sum_i R_i, \quad (2.30)$$

where R_i are individual thermal resistances.

2.4 Estimating heat transfer coefficient

As was mentioned in previous section, *heat transfer coefficient* h describes proportionality between heat transfer and temperature difference between surface and bulk fluid (see equation (2.15)). Heat transfer coefficient is often evaluated from dimensionless *Nusselt number* Nu , which is a ratio of convective to conductive heat transfer in the fluid.

$$Nu = \frac{h}{kL_c}, \quad (2.31)$$

where Nu is Nusselt number, h is convection heat transfer coefficient, k is thermal conductivity of fluid and L_c is characteristic length.

Because experimental correlations are used to evaluate Nusselt number, it is extremely important to correctly identify type of fluid flow, with which we are dealing with and choose the right correction for that situation.

Below few most important categories distinguished by different properties are listed:

1. (a) Internal flow - flow confined in a channel (pipe, duct)
 - (b) Open-channel flow - flow in channel, where liquid has a free surface (river)
 - (c) External flow - flow over a surface (air over a wing)
2. (a) Natural flow - flow is driven by buoyancy
 - (b) Forced flow - fluid is forced to flow by external means (pump)

3. (a) Compressible flow - density of fluid does not change (typically liquids)
 (b) Incompressible flow - density of fluid does change (typically gases at high velocities)
4. (a) Laminar flow - ordered flow, velocity streamlines are smooth
 (b) Turbulent flow - disordered flow, random fluctuations of velocity
 (c) Transitional flow - flow alternating between laminar and turbulent
5. (a) Single-phase flow - only one state of fluid
 (b) Two-phase flow - two phases are present (water and water vapor)

In ITER FW fingers cooling water flows in tubes propelled by pumps, clearly, the flow is forced, incompressible and internal. It will be shown that flow is turbulent for all values of mass flow rate given in section 1.4.

2.4.1 Internal forced convection with turbulent flow

Fluid flowing over a surface develops a velocity profile perpendicular to the surface. The cause of this is the no-slip condition at the surface, where the fluid velocity is zero and then the bulk flow velocity at the fluid core. It is convenient to substitute this profile with just one value called *mean velocity* v , which is the average velocity along the profile.

Similarly, there is a thermal profile, when the fluid flows across surface of different temperature than its bulk temperature. Also thermal profile can be substituted with one value constant over the tube cross section – the *mean temperature* T_m .

It takes some time before these profiles develop behind an inlet in a tube. The distance is called a *hydrodynamic entry length* L_h for velocity and a *thermal entry length* L_t for temperature. For turbulent flow, they are approximately equal and can be estimated as

$$L_h = L_t \cong 10D, \quad (2.32)$$

where D is the inner diameter of the tube.

Most of experimental correlations used to determine Nusselt Nu number for forced convection are in form

$$Nu = f(Pr, Re), \quad (2.33)$$

where Pr is Prandtl number and Re is Reynolds number.

Prandtl number Pr is ratio of diffusivity of momentum to diffusivity of heat.

$$Pr = \frac{\nu}{\alpha}, \quad (2.34)$$

where ν is kinematic viscosity and α is thermal diffusivity of the fluid.

Substituting from definition of thermal diffusivity (2.9) and from the definition of kinematic viscosity ν

$$\nu = \frac{\mu}{\rho}, \quad (2.35)$$

where μ is dynamic viscosity and ρ is mass density of the fluid,

$$Pr = \frac{\mu c_p}{k}, \quad (2.36)$$

where c_p is specific heat capacity at constant pressure and k is thermal conductivity of the fluid.

Higher Prandtl number means that heat diffuses quicker than momentum.

Reynolds number Re is ratio of inertial to viscous forces and its value predicts if the flow will be laminar or turbulent. Reynolds number is defined as

$$Re = \frac{vL_c}{\nu} = \frac{\rho v L_c}{\mu}, \quad (2.37)$$

where v is mean velocity, L_c is characteristic length of the flow channel, ν is kinematic viscosity and μ is dynamic viscosity.

Generally, flow is considered laminar if $Re < 2300$, transitional if $2300 < Re < 10000$ and turbulent for $Re > 10000$. [2]

For internal convection, the characteristic length L_c , in both expressions for Nusselt number (2.31) and for Reynolds number (2.37), is *hydraulic diameter* D_h calculated using formula:

$$D_h = \frac{4A_c}{p}, \quad (2.38)$$

where A_c is cross-sectional area of the tube and p is wetted perimeter.

In case of circular tube of inner diameter D :

$$D_h = \frac{4\pi(\frac{D}{2})^2}{2\pi\frac{D}{2}} = D. \quad (2.39)$$

Equation for Reynolds number (2.37) can be then rewritten in terms of mass flux G .

$$Re = \frac{\rho v D}{\mu} = \frac{\rho D}{\mu} \left(\frac{G}{\rho \pi (\frac{D}{2})^2} \right) = \frac{4G}{\mu \pi D}. \quad (2.40)$$

The most common correlation for turbulent flow is Dittus-Boelter correlation [6]:

$$Nu = \begin{cases} 0.024 Re^{0.8} Pr^{0.4} & \text{for heating} \\ 0.026 Re^{0.8} Pr^{0.3} & \text{for cooling} \end{cases}, \quad (2.41)$$

where Re is Reynolds number and Pr is Prandtl number. Dittus-Boelter correlation is valid for $0.7 < Pr < 120$ and $2500 < Re < 124000$.

Higher accuracy (below 10 %) can be achieved by using more complex correlation like *Gnielinski correlation* [2]:

$$Nu = \frac{(\frac{f}{8}) \cdot (Re - 1000) \cdot Pr}{1 + 12.7 \cdot (\frac{f}{8})^{0.5} \cdot (Pr^{\frac{2}{3}} - 1)}, \quad (2.42)$$

where f is friction factor, Re is Reynolds number, and Pr is Prandtl number. This correlation is valid for $0.5 < Pr < 2000$ and $3000 < Re < 5 \times 10^6$.

The friction factor f of a tube with smooth surface can be determined from *first Petukhov equation* [2].

$$f = (0.79 \cdot \ln(Re) - 1.64)^{-2}, \quad (2.43)$$

where Reynolds number Re is in range $3000 < Re < 5 \times 10^6$.

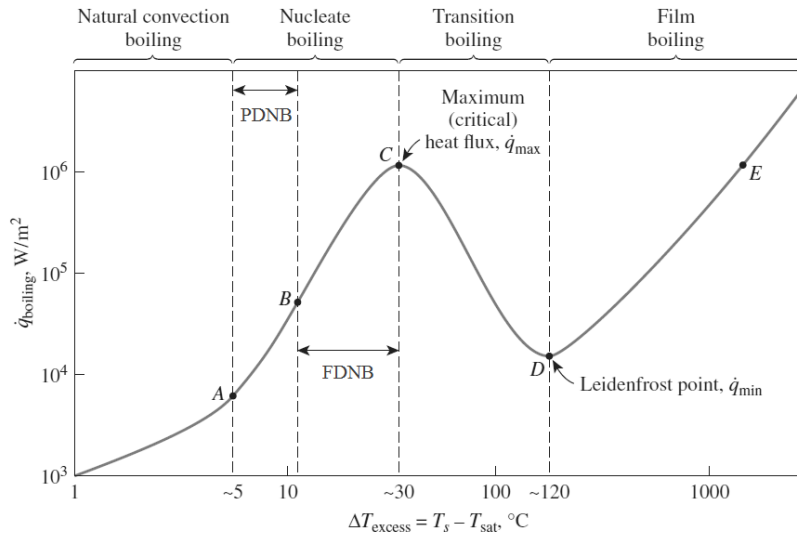


Figure 2.1: Typical boiling curve. Water at 1 atm. Dependency of boiling heat flux \dot{q}_{boiling} on surface superheat ΔT_{excess} . [2]

2.4.2 Flow boiling

The situation gets more complicated when tube surface exceeds saturation temperature of liquid T_{sat} . The liquid might evaporate at the tube surface, the vapor bubbles enter the flow, which then becomes two-phase. boiling at the surfaces becomes possible and in that case, flow might become two-phase. It is worth noting that boiling may occur whether the mean temperature is higher than saturation temperature or not.

If the mean temperature is lower than saturation temperature, the vapor bubbles condense once they reach colder main flow and we call the boiling *subcooled*. If it is equal to saturation temperature, it is referred to as *saturated boiling*. [5]

Many heat transfer mechanisms are possible in boiling, they are differentiated by various boiling regimes. *Boiling curve* (such as in figure 2.1) is a nice representation of these regimes.

Forced convection up to point *A* in the figure 2.1

Evidence suggests that some degree of wall superheat is required for boiling. Up to that point heat transfer is by single-phase convection and is strongly affected by fluid velocity and temperature.

Nucleate boiling from point *A* to point *C* in the figure 2.1

Point *A* is referred to as *onset of nucleate boiling - ONB*. It is associated with surface temperature T_{ONB} - *temperature of onset of nucleate boiling* - and heat transfer \dot{q}_{ONB} . At these conditions, the wall superheat is large enough to support bubble formation and growth at nucleation sites. As the bubbles depart from the surface, they carry heat and also increase turbulence.

At first, isolated bubbles appear variously on the surface and heat transfer is combination of forced convection and boiling, affected both by local conditions at the wall and bulk fluid properties. This sub regime is called *Partial developed nucleate boiling PDNB*.

When the wall superheat is increased, specifically, above *Onset of fully-developed nucleate boiling - OFDNB* (see point *B* in the fig. 2.1), bubble density rapidly grows and bubbles form all along the surface, which greatly increases turbulences and consequently, mixing. This mechanism is therefore detached from the main flow and is dominated by conditions at the wall, it is referred to as *Fully developed nucleate boiling FDNB*.

However, when the bubble density becomes large enough to cover most of the surface, the vapor bubbles block fluid from reaching the surface and create barrier. Since gases usually have much lower thermal conductivity than liquids, this leads to significant reduction of heat transfer. The point at which this occurs is called *Departure from nucleate boiling DNB* and the associated heat flux is called *Critical heat flux CHF*. On the boiling curve in the fig. 2.1 it is represented by point *C*.

Transition film boiling from point *C* to point *D* in the figure 2.1

As more and more of the surface is covered with insulating vapor patches, the heat transfer continues to plummet. This region is called *Transition film boiling* or sometimes *Partial film boiling*.

Film boiling from point *D* onwards in figure 2.1

The point *D* in the figure 2.1 is called *Leidenfrost point* and it marks the moment when whole surface is covered by vapor film. The heat transfer reaches minimum and begins to rise again with higher excess temperature. The mechanism involve conduction and convection in vapor film at the surface and evaporation at the vapor-fluid interface.

In reality, steady operation beyond the point of critical heat flux is only possible in systems with controlled wall temperature. If the system regulates heat flux, the rise of heat flux beyond the critical heat flux causes increase in wall temperature, which in turn, leads to greater coverage of the surface by the vapor film, insulating the surface and obstructing heat transfer. This chain reaction manifest itself with a jump on boiling curve from the point *C* to the point *E* in film boiling region (see fig. 2.1), where the new heat flux is possible.

On one hand, nucleate boiling regime is very useful, because it provides great enhancement of heat transfer with just small increment in wall temperature. On the other, it is equally important to beware of reaching the critical heat flux with which a tremendous and quick rise of wall temperature is associated.

Engineering safety limit for maximum heat flux is used to prevent the system from reaching the critical heat flux and departure from nucleate boiling. It is often represented with *Departure from nucleate boiling ration DNBR*.

$$DNBR = \frac{\dot{q}_{CHF}}{\dot{q}}, \quad (2.44)$$

where \dot{q}_{CHF} is critical heat flux and \dot{q} is heat flux.

Usually, the DNBR is required to satisfy

$$DNBR > 1.3. \quad (2.45)$$

With this in mind, in case of ITER FW fingers, only partially and fully developed nucleate boiling can be allowed to occur. Given that mean outlet water temperature is supposed to be under $110\text{ }^\circ\text{C}$ and that saturation temperature for water at 3 MPa is approximately $233\text{ }^\circ\text{C}$, any boiling will be highly subcooled.

Bergles-Rohsenow correlation can be used for calculation of the temperature of onset of nucleate boiling T_{ONB} in water. [12]

$$T_{ONB} = T_{sat} + 0.556 \left(\frac{\dot{q}_{ONB}}{1082p^{1.156}} \right)^{0.046p^{0.0234}}, \quad (2.46)$$

where T_{sat} is saturation temperature, \dot{q}_{ONB} is heat flux of onset of nucleate boiling and p is water pressure in *bar*. It is applicable for pressures from 1 to 138 *bar*.

\dot{q}_{ONB} must satisfy also equation for forced convection

$$\dot{q}_{ONB} = h_{FC}(T_{ONB} - T_m), \quad (2.47)$$

where h_{FC} is forced convection heat transfer coefficient, T_{ONB} is surface temperature at the wall and T_m is mean temperature.

These two equations together form a system of non-linear equations, which after solving gives values of T_{ONB} and \dot{q}_{ONB} .

One of the most popular correlations available for fully-developed nucleate boiling in water is *Thom correlation*. [15]

$$T_w = T_{sat} + 22.5(\dot{q}_{FDNB} \cdot 10^{-6})^{\frac{1}{2}} e^{-\frac{p}{87}}, \quad (2.48)$$

where T_w is surface temperature at the wall, T_{sat} is saturation temperature, \dot{q}_{FDNB} is heat flux and p is water pressure in *bar*. It is applicable to pressures up to 200 *bar*.

Rewritten in terms of wall superheat:

$$\dot{q}_{FDNB} = 10^6 \left(\frac{e^{\frac{p}{87}}}{22.5} \right)^2 (T_w - T_{sat})^2. \quad (2.49)$$

Between single-phase convection and fully-developed boiling lies the partially-developed nucleate boiling region. Because it combines two different mechanisms of heat transfer, the correlations often combine heat transfer models or correlations for forced convection and FDNB. One of them was proposed by Bergles and Rohsenow [1] and leads to expression for heat flux \dot{q} dependency

$$\dot{q} = \dot{q}_{FC} \left[1 + \left(\frac{\dot{q}_{NB} \dot{q}_{NB} - \dot{q}_{NB}(T_{ONB})}{\dot{q}_{FC} \dot{q}_{NB}} \right)^2 \right]^{\frac{1}{2}} \quad (2.50)$$

where \dot{q}_{FC} is forced convection heat flux, \dot{q}_{NB} is fully-developed nucleate boiling heat flux and $\dot{q}_{NB}(T_{ONB})$ is fully-developed nucleate boiling heat flux evaluated at temperature of onset of nucleate boiling T_{ONB} .

This equation can be reduced to

$$\dot{q} = [\dot{q}_{FC}^2 + (\dot{q}_{NB} - \dot{q}_{NB}(T_{ONB}))^2]^{\frac{1}{2}}. \quad (2.51)$$

This expression is also applicable both to forced convection and fully-developed nucleate boiling regions. Convective heat transfer coefficient h can be evaluated as

$$h = \frac{\dot{q}}{(T_w - T_m)}, \quad (2.52)$$

where \dot{q} is heat flux from equation (2.51), T_w is wall temperature and T_m is mean temperature of water.

Substituting from (2.42) and (2.49) to (2.51) and then to (2.52), the equation for convection heat transfer coefficient is obtained

$$h = \frac{\left[(h_{FC}(T_w - T_m))^2 + \left(10^6 \left(\frac{(e^{87})}{22.5} \right)^2 (T_w - T_{sat})^2 - 10^6 \left(\frac{(e^{87})}{22.5} \right)^2 (T_{ONB} - T_{sat})^2 \right)^2 \right]^{\frac{1}{2}}}{(T_w - T_m)}, \quad (2.53)$$

where h_{FC} is forced convection heat transfer coefficient, T_w is wall temperature, T_m is mean temperature of water, T_{sat} is saturation temperature of water, p is water pressure in *bar* and T_{ONB} is temperature of onset of nucleate boiling.

Seeing that equation (2.53) is non-linear in T_w , it is not trivial to express the wall temperature explicitly.

In *Assessment of correlations and models for the prediction of CHF in water subcooled flow boiling* [3] Celata et al. suggest *modified Tong-68 correlation* for calculating critical heat flux \dot{q}_{CHF} in conditions relevant to fusion reactors.

$$\dot{q}_{CHF} = Ch_{lv} \sqrt{\frac{G\mu}{D}}, \quad (2.54)$$

$$C = (0.216 + 4.74 \times 10^{-8} p) \psi, \quad (2.55)$$

$$\psi = \begin{cases} 1 & \chi_e < -0.1 \\ 0.825 + 0.986\chi_e & -0.1 < \chi_e < 0 \\ \frac{1}{2+30\chi_e} & \chi_e > 0 \end{cases}, \quad (2.56)$$

where h_{lv} is latent heat of water-steam phase change, G is mass flux density, D is inner diameter of the tube and χ_e is equilibrium vapor quality.

Vapor quality is mass fraction of vapor in a vapor-liquid mixture. Saturated liquid has a quality of 0 and saturated vapor of 1. In equilibrium, quality can be calculated using

$$\chi_e = \frac{h - h_l}{h_{lv}}, \quad (2.57)$$

where h is specific enthalpy, h_l is enthalpy of saturated liquid and h_{lv} is latent heat of water-steam phase change.

However, if the system is not in thermal equilibrium (subcooled boiling or small droplets of liquid dispersed in overheated vapor), this formula can give results out of 0-1 range and the quantity is called *equilibrium quality* χ_e .

Chapter 3

Heat transfer analysis of ITER FW06A panel

FW06A is a NHF FW panel designed for use in ITER. It was chosen as a representative panel, because some other studies have been already performed on this design [23]. As is shown in the fig. 3.1, this panel is 1001 mm high and 1385 mm wide. 48 fingers are mounted to the I-beam, 24 on each side. The fingers are grouped by 3 to hydraulic channels connected through the I-beam to inlet and outlet pipes and subsequently, to the blanket manifold. The coolant flow geometry for 2 channels (6 fingers) and the internal structure of the I-beam are illustrated in the fig. 3.2. The coolant flow is more apparent from the cross-sectional view in fig. 3.3, which demonstrates how one hydraulic channel cools 3 fingers.

3.1 Description

A single finger is 41 mm wide, 695 mm long and 66 mm thick and it consists of several layers, as you can see in the fig. 3.4. The structural support is provided by stainless steel 316L backing plate, through which runs 26 mm diameter tube. Onto the backing plate, a CuCrZr alloy heat sink layer is joined. Two $11/12\text{ mm}$ diameter SS316L tubes are embedded into the CuCrZr layer. The plasma facing surface is made of beryllium tiles. Between the Be tiles and

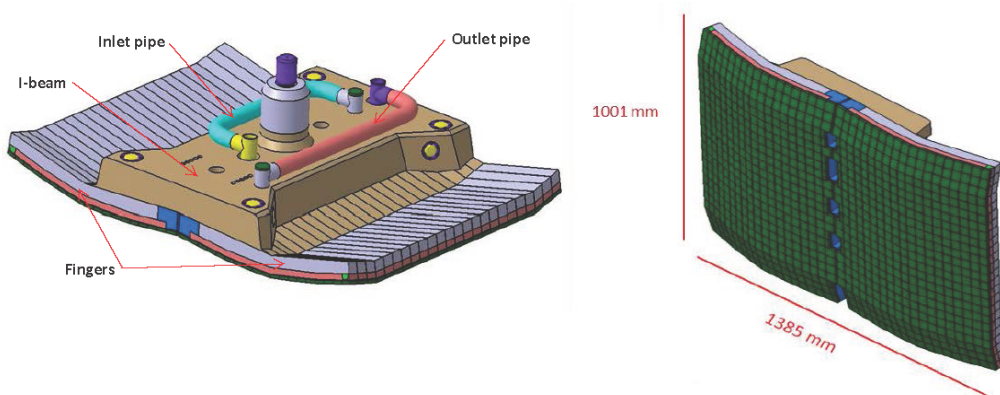


Figure 3.1: ITER FW panel type FW06A. [8]

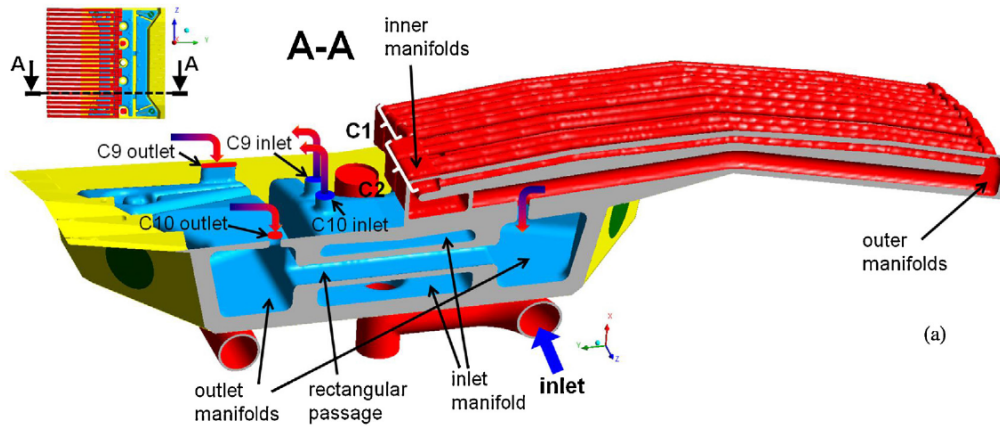


Figure 3.2: Coolant flow geometry for two channels $C1$, $C2$ and their hydraulic connection to the I-beam. [23]

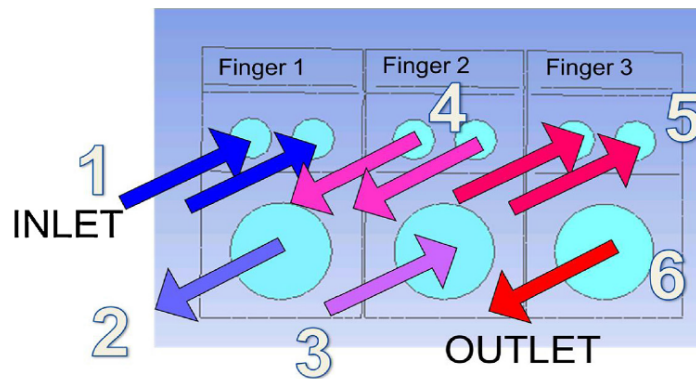


Figure 3.3: Coolant flow through channel in cross-sectional view with ordered numbering of corresponding hydraulic paths. Color represents heating of the coolant (blue is colder, red is hotter).[23]

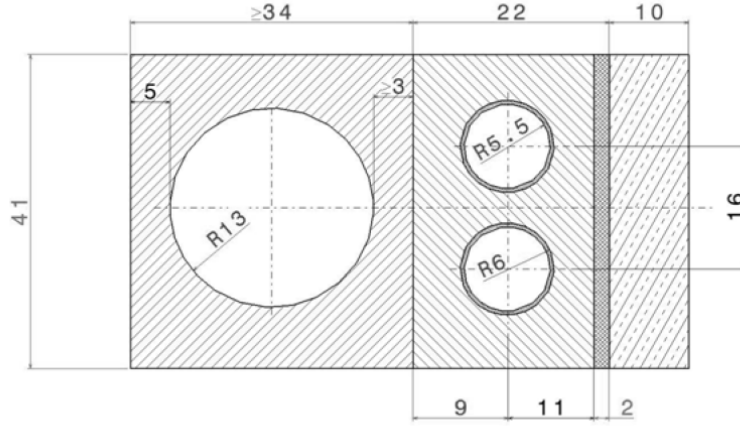


Figure 3.4: Cross-section of the FW06A finger at generic level. [11]

the CuCrZr layer is 2 mm thick copper compliant layer, which reduces thermal stresses.

3.1.1 Materials

The description and properties of materials used in ITER FW panels are provided in *ITER structural design criteria for in-vessel components, Appendix A - Materials design limit data* [14]. The support backing plate and the embedded tubes are made of austenitic *stainless steel type 316L(N)-IG*. The maximum allowable temperature is 600 °C without irradiation and 450 °C with irradiation up to 10 dpa. The thermal conductivity k_{SS316L} in range from 20 °C to 500 °C is given by equation:

$$k_{SS316L} = 0.014337T + 13.561, \quad (3.1)$$

where T is temperature in centigrade. For visual representation see fig. 3.5.

Copper alloy *CuCrZr-IG* is used as a heat sink. The chemical composition in weight percentage: balance to 100 % copper, 0.6 – 0.8 % chrome, 0.07 – 0.15 % zirconium, < 0.01 % impurities. Maximum temperature should not exceed 450 °C. The thermal conductivity k_{CuCrZr} in range from 20 °C to 500 °C is given by equation:

$$k_{CuCrZr} = -2.2918 \cdot 10^{-7}T^3 + 4.5872 \cdot 10^{-4}T^2 - 2.2465 \cdot 10^{-1}T + 383.20, \quad (3.2)$$

where T is temperature in centigrade. For visual representation see fig. 3.6.

The compliance layer is made of dispersion-strengthened copper alloy *CuAl25-IG*, where Al25 points to the original *Glidcop®Al-25, LOX-80, CR process* alloy and *IG* stands for *ITER grade*. The chemical composition in weight percentage: 99.5 % copper, 0.48 % aluminum oxide, the rest is boron oxide (product of reducing oxygen content, elemental boron binds oxygen that was previously free or combined with copper) and impurities. The thermal conductivity k_{Cu} in range from 20 °C to 500 °C is given by equation:

$$k_{Cu} = -7.2083 \cdot 10^{-9}T^3 + 3.1483 \cdot 10^{-4}T^2 - 2.6371 \cdot 10^{-1}T + 350.28, \quad (3.3)$$

where T is temperature in centigrade. For visual representation see fig. 3.7.

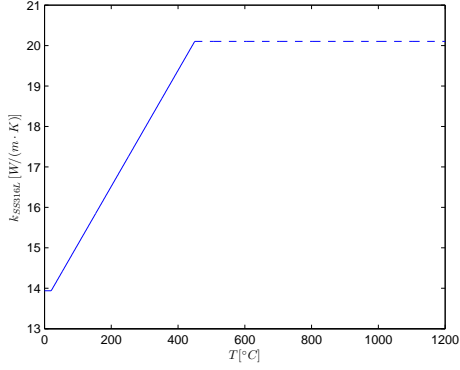


Figure 3.5: Thermal conductivity of SS316L. Dashed region is extrapolation beyond defined values.

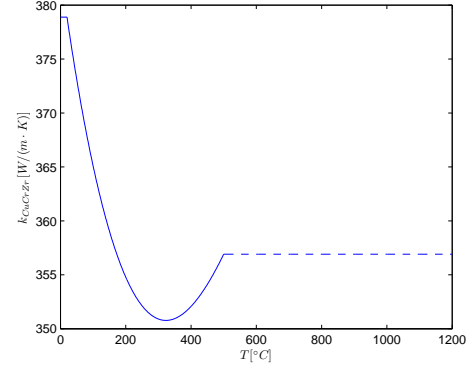


Figure 3.6: Thermal conductivity of CuCrZr alloy. Dashed region is extrapolation beyond defined values.

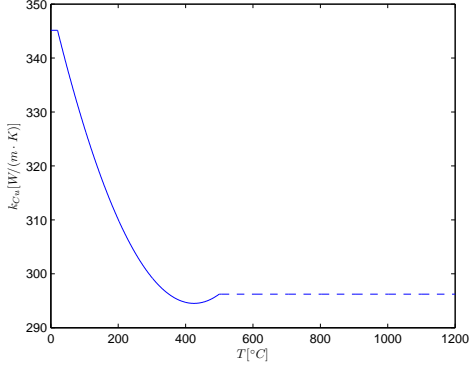


Figure 3.7: Thermal conductivity of copper. Dashed region is extrapolation beyond defined values.

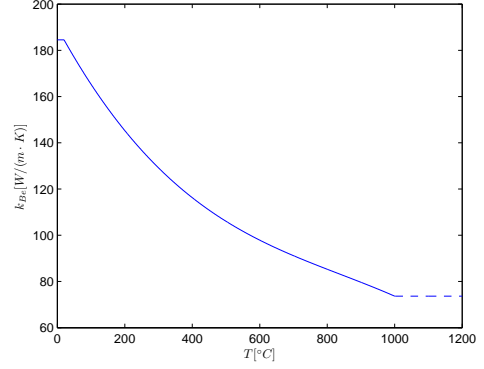


Figure 3.8: Thermal conductivity of beryllium. Dashed region is extrapolation beyond defined values.

The beryllium tiles are manufactured from *Beryllium S-65C VHP (Vacuum Hot Pressed)*. The minimal Be content is 99 %. The thermal conductivity k_{Be} in range from 20 °C to 1000 °C is given by equation:

$$k_{Be} = -1.0104 \cdot 10^{-7}T^3 + 2.5429 \cdot 10^{-4}T^2 - 0.25429 \cdot 10^{-1}T + 189.8, \quad (3.4)$$

where T is temperature in centigrade. For visual representation see fig. 3.8.

The comparison of the thermal conductivities of these materials is in fig. 3.9.

The properties of cooling water were obtained from International Association for Properties of Water and Steam Industrial Formulation 1997 (IAPWS IF-97) via the XSteam function for MathWorks Matlab by Magnus Holmgren.

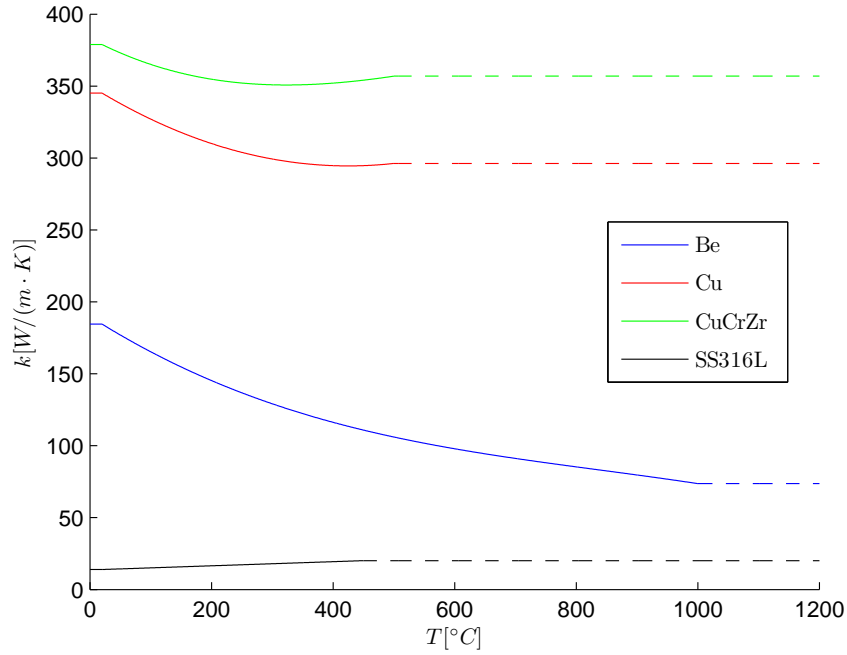


Figure 3.9: Comparison of thermal conductivities of materials. Dashed regions are extrapolations beyond defined values for each material.

3.1.2 Simplifications

Number of simplifications were made to model the real situation.

Geometry - The FW06A panel is composed of 16 individual hydraulic channels, each of them comprising 3 fingers. I simulated one such channel. Furthermore, the channel has hydraulic connections to inlet and outlet pipes and between the fingers. These connections were neglected for the sake of simplicity as well as any curvature of the fingers and the gaps between individual beryllium tiles. The hydraulic channel was straightened to a single long finger of constant cross-section with length of 3 original fingers (see fig. 3.10).

On top of that, the lower 26 mm tube does not contribute much to the extraction of heat and was replaced with insulating boundary condition (2.13) at the SS316 and CuCrZr layers interface. The remaining structure with two 11 mm tubes is symmetric and it is sufficient to model just a half of it, substituting the other half with an insulated boundary condition at the plane of the symmetry as is shown in the fig. 3.11.

Uniform heat flux - In reality, the heat flux will have a profile across poloidal direction caused by particles hitting the plasma facing surface under an angle due to the magnetic field lines that they follow, and also due to the curvature of the fingers in some types of panels. Because no profiles for testing in HELCZA were yet available, I used an uniform heat flux profile.

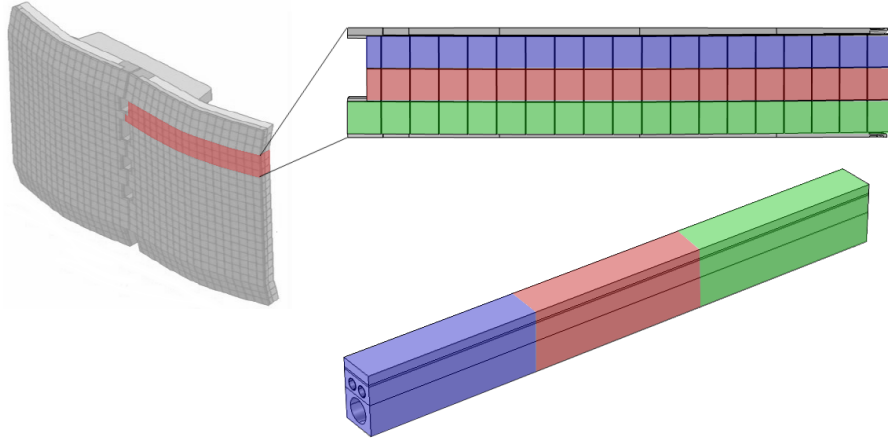


Figure 3.10: Illustration of how a three-finger channel is straightened to a single finger of constant cross-section.

Steady-state heat transfer - Although, the heat transfer in the panel during the operation of ITER and testing in HELCZA will be transient, I chose to perform steady-state heat transfer analysis, because it is an adequate approximation and it is significantly faster to compute.

3.2 General thermal analysis

My task was to estimate heat transfer through ITER FW panels for

- heat flux density \dot{q} in range $(0.5 - 4.7) \text{ MW/m}^2$,
- cooling water mass flow rate through the whole panel \dot{m}_{total} in range $(1 - 15) \text{ kg/s}$, which corresponds to a mass flow rate for one channel \dot{m} : $\frac{(1 - 15)}{16} = (0.0625 - 0.9375) \text{ kg/s}$.

The panel is cooled by water pressurized to 3 MPa with inlet temperature $70 \text{ }^\circ\text{C}$, the outlet temperature is required to be under $110 \text{ }^\circ\text{C}$. If we set the outlet temperature to be the limit we try to comply with and assume steady-state, no heat generation situation we can use equation (2.3) to calculate thermal equilibrium:

$$\dot{q}(3W + 2W_{\text{gap}})l = \dot{m}c_{p_{\text{water}}}(T_e - T_i), \quad (3.5)$$

where \dot{q} is heat flux density, W is finger width, W_{gap} is width of gap between fingers, l is length of irradiated part of the fingers, \dot{m} is mass flow rate through one channel, $c_{p_{\text{water}}}$ is specific heat capacity of water and T_e, T_i are outlet, resp. inlet temperatures.

The specific heat capacity of water (all the other water properties as well) is evaluated at the bulk temperature T_b , which is arithmetical average of the mean temperatures at the inlet T_i and at the outlet T_e .

$$T_b = \frac{T_i + T_e}{2} = \frac{70 + 110}{2} = 90^\circ\text{C}. \quad (3.6)$$

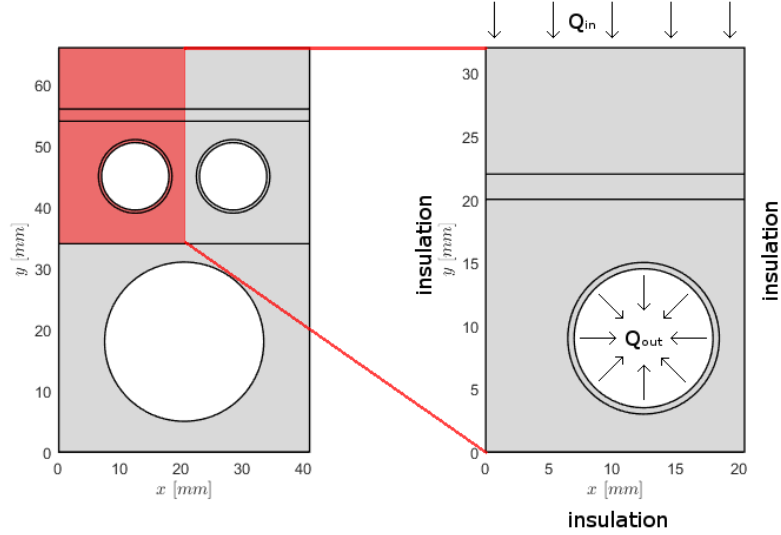


Figure 3.11: Overview of model setup in cross-sectional view with depicted boundary conditions.

Rearranging the (3.5) for expression for maximum allowable length of irradiated area l yields

$$l = \frac{\dot{m}c_{p_{\text{water}}}(T_e - T_i)}{\dot{q}(3W + 2W_{\text{gap}})}. \quad (3.7)$$

Channels longer than l will have outlet temperature greater than $110\text{ }^\circ\text{C}$ and will not satisfy the condition for the outlet temperature. In the fig. 3.12, the values above the length of the finger L allow the whole finger to be heated. This is better represented in the fig. 3.13, where you can see that for high heat flux and low mass flow, only small fragment of the panel can be heated, and for low heat flux, high mass flow, whole panel can be irradiated. In any subsequent calculations the channel length will be replaced with this maximum allowable channel length to guarantee that the outlet temperature will not exceed $110\text{ }^\circ\text{C}$.

3.2.1 Convective heat transfer coefficient

To determine the convective heat transfer coefficient h , the coolant flow must be investigated first. The water properties at the temperature $T_b = 90\text{ }^\circ\text{C}$ and at the pressure of 3 MPa are

- saturation temperature $T_{\text{sat}} = 233.86\text{ }^\circ\text{C}$
- specific heat capacity $c_{p_{\text{water}}} = 4198.6\text{ J}/(\text{kg} \cdot \text{K})$
- density $\rho_{\text{water}} = 966.64\text{ kg}/\text{m}^3$
- dynamic viscosity $\mu_{\text{water}} = 3.152 \cdot 10^{-4}\text{ Pa} \cdot \text{s}$

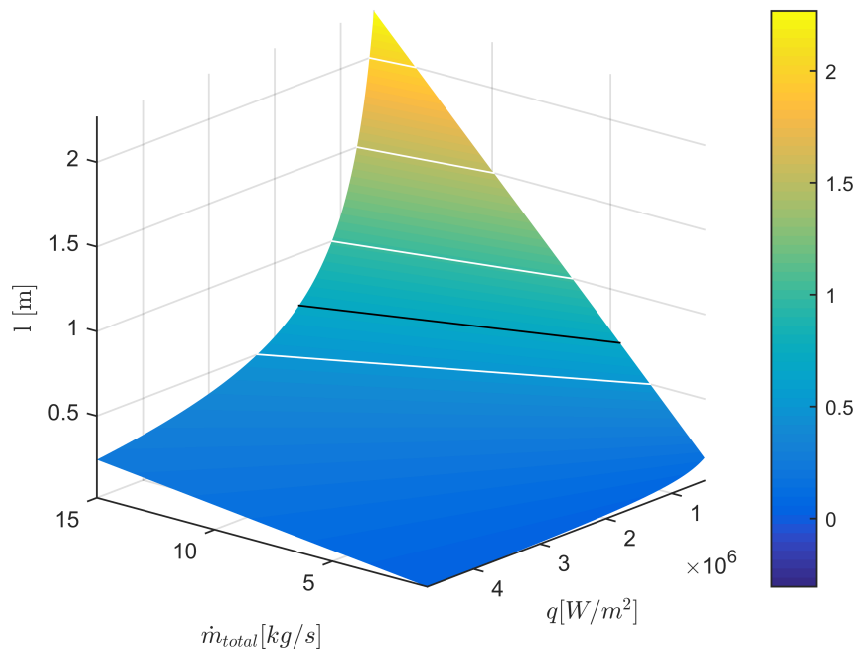


Figure 3.12: Maximum allowable length of irradiated area of the channel. Black is the actual length of the channel.

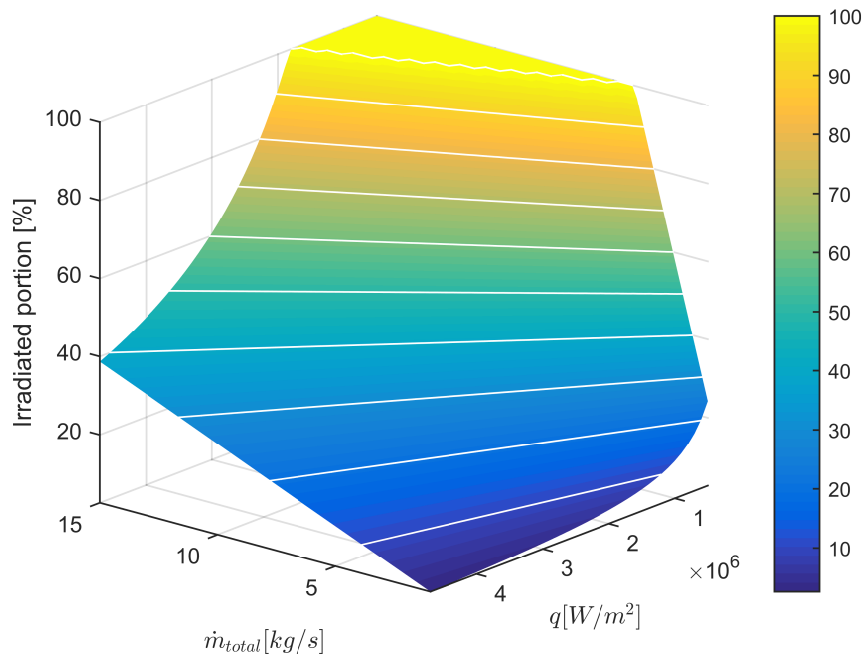


Figure 3.13: Maximum allowable percentage of the total area of the finger to be irradiated, to ensure outlet temperature is below $110\text{ }^{\circ}\text{C}$.

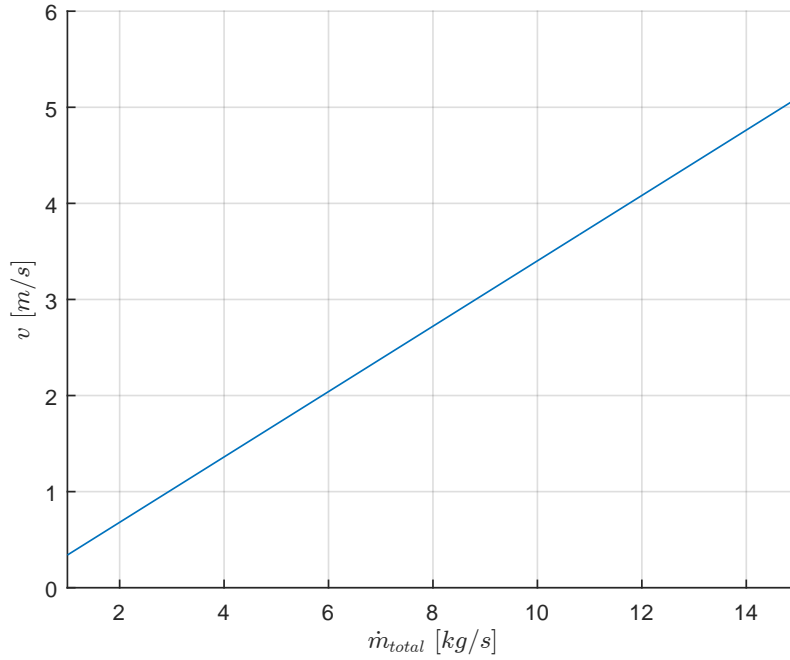


Figure 3.14: Water coolant velocity in the 11 mm diameter pipe over the mass flow rate parameter.

- thermal conductivity $k_{\text{water}} = 0.6746 \text{ W}/(\text{m} \cdot \text{K})$

If the mass flow rate through the channel \dot{m} is in range $(0.0625 - 0.9375) \text{ kg/s}$ and the water flows through two circular pipes with diameter d of 11 mm, then the coolant velocity v can be calculated as

$$v = \frac{\dot{m}}{\rho_{\text{water}} 2\pi \left(\frac{d}{2}\right)^2}. \quad (3.8)$$

In the fig. 3.14, the velocities corresponding to the mass flow rate are represented.

Using equation (2.37), the Reynolds number for different flows can be obtained. As is apparent from figure 3.15, the Reynolds number exceeds value of 10,000 for whole range of mass flow rate parameters. This means that the flow is in all cases turbulent.

Prandtl number Pr obtained from equation (2.34) is 1.9617. The values of both Prandtl and Reynolds number enable to use the Gnielinski correlation (2.42) and the first Petukhov equation (2.43) to calculate Nusselt number Nu for the whole range of mass flow rate. From the Nusselt number the convective heat transfer coefficient for forced convection h_{FC} can be calculated using equation (2.31). The resulting values are illustrated in the fig. 3.16 for Nusselt number Nu , respectively in fig. 3.17 for forced convection heat transfer coefficient h_{FC} .

It is possible that the local water temperature will rise enough that the water starts boiling. To detect this case, it is necessary to know the temperature of onset of nucleate boiling T_{ONB} . It can be obtained by solving system of equations for Bergles-Rohsenow correlation (2.46) and

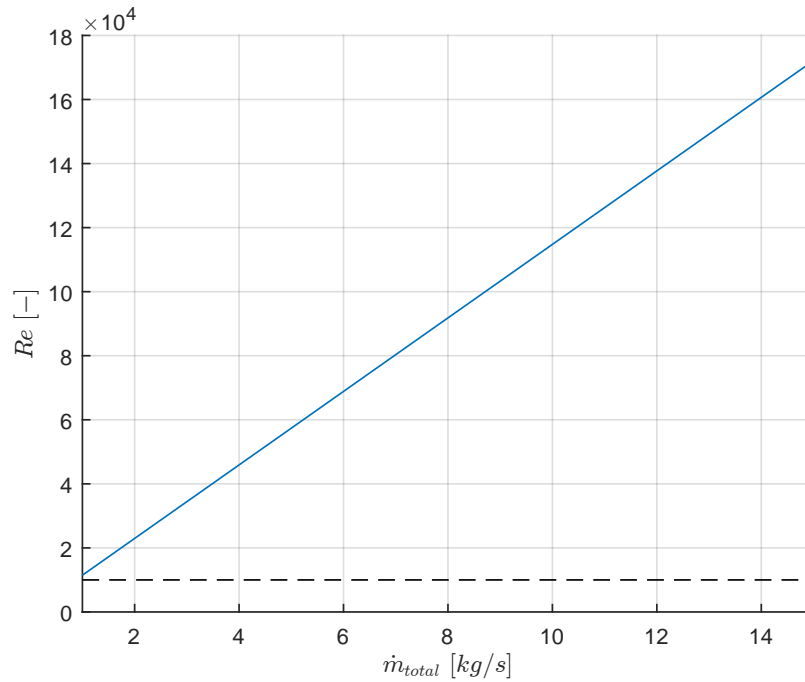


Figure 3.15: Dependency of Reynolds number Re of water flow in the 11 mm diameter pipe on the mass flow rate parameter \dot{m}_{total} . The black dashed line at 10000 represents lower limit for turbulent flow.

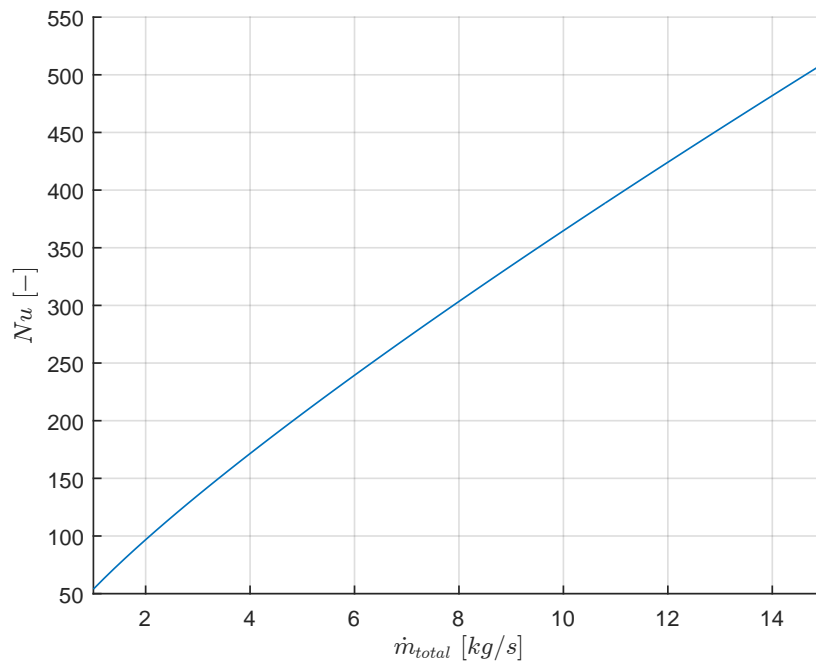


Figure 3.16: Nusselt number Nu acquired from Gnielinski correlation over the mass flow rate parameter \dot{m}_{total} .

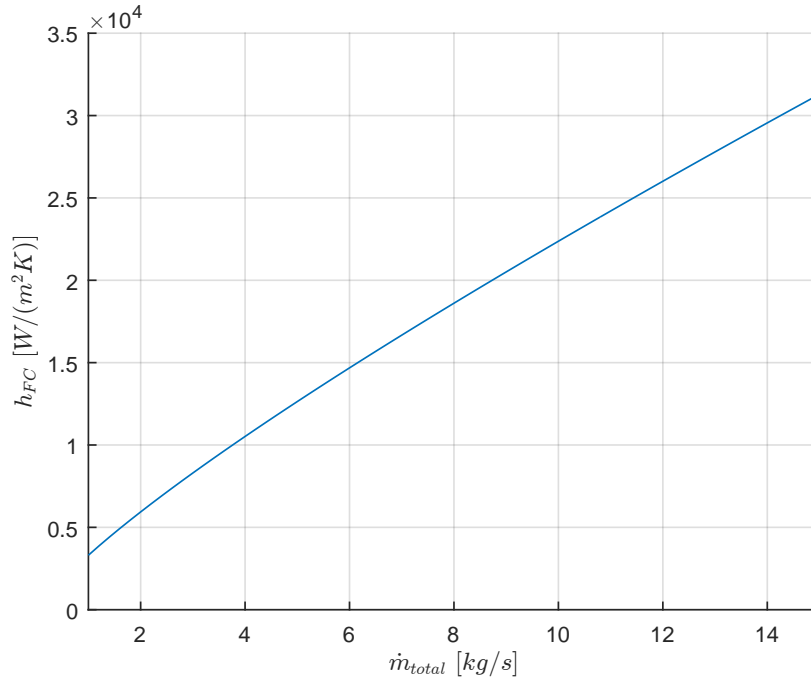


Figure 3.17: Convective heat transfer coefficient for forced convection h_{FC} over the mass flow rate parameter \dot{m}_{total} .

for corresponding forced convection heat flux (2.47). The T_{ONB} is represented in the fig. 3.18 and is approximately 2 – 5 °C higher than the saturation temperature $T_{sat} = 233.86$ °C.

The *modified Tong-68 correlation* (2.56) is used to calculate critical heat flux \dot{q}_{CHF} and the result is illustrated in fig. 3.19.

The equation (2.53) determines the corresponding convective heat flux \dot{q} for a wall temperature T_w . Fig. 3.20 shows comparison of this heat flux, which is calculated using the *Bergles-Rohsenow method* (2.51), with forced convection heat flux \dot{q}_{FC} from *Gnielinski correlation* (2.42) and the fully developed nucleate boiling heat flux \dot{q}_{FDNB} from *Thom correlation* (2.49). It is important that the heat flux \dot{q} does not exceed the *departure from nucleate boiling limit DNB* (2.44), where the critical heat flux $\dot{q}_{CHF} = 1.3 \dot{q}$.

Similarly, the convective heat transfer coefficient h dependency on wall temperature T_w is illustrated in fig. 3.21. It is apparent that the boiling greatly increases the cooling capability, because even slight increment in wall superheat in the boiling regime is accompanied with huge rise in the heat transfer coefficient value.

3.3 1D model

I started with 1D model to have a reference for the more complicated 2D and 3D models. The 1D model calculates temperatures at the end of the channel, where mean coolant temperature is $T_m = T_e = 110$ °C, and on the shortest line connecting beryllium surface and the cooling tube. This line is depicted in the fig. 3.22. The problem can be classified as one-dimensional steady-state conduction with a constant heat flux boundary condition (2.12) on one side and a convection boundary condition (2.15) on the other.

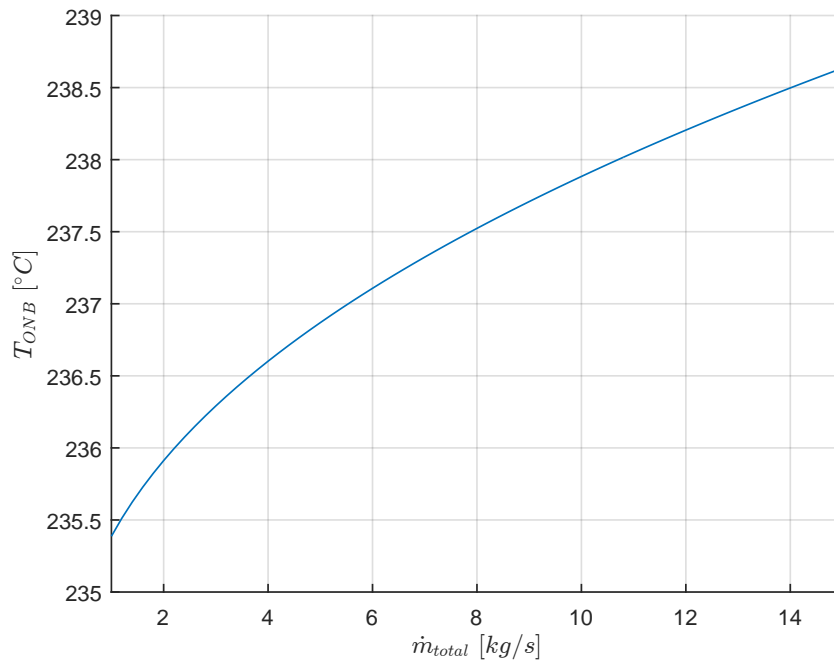


Figure 3.18: Temperature of onset of nucleate boiling T_{ONB} over the mass flow rate parameter \dot{m}_{total} . The saturation temperature is $233.86\text{ }^{\circ}\text{C}$.

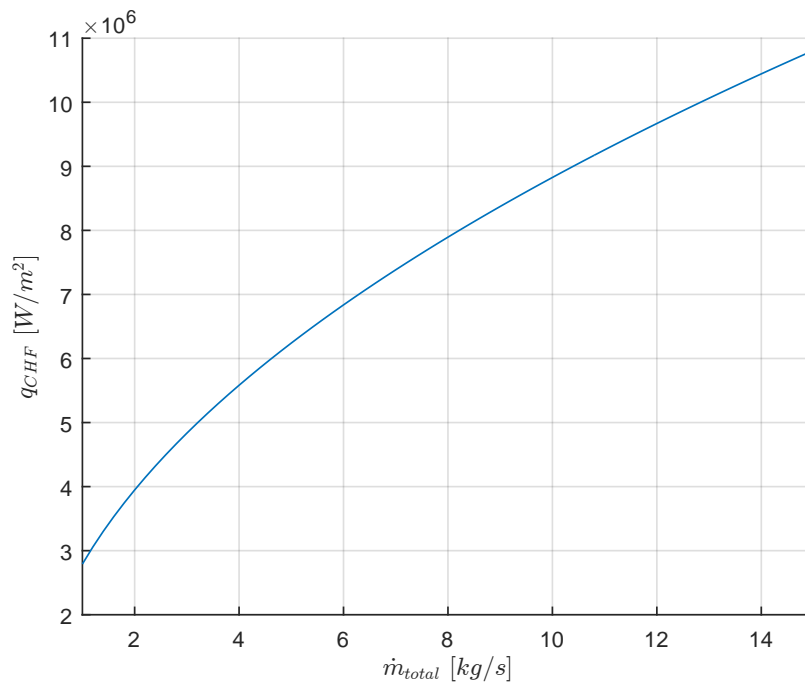


Figure 3.19: Critical heat flux \dot{q}_{CHF} over the mass flow rate parameter \dot{m}_{total} .

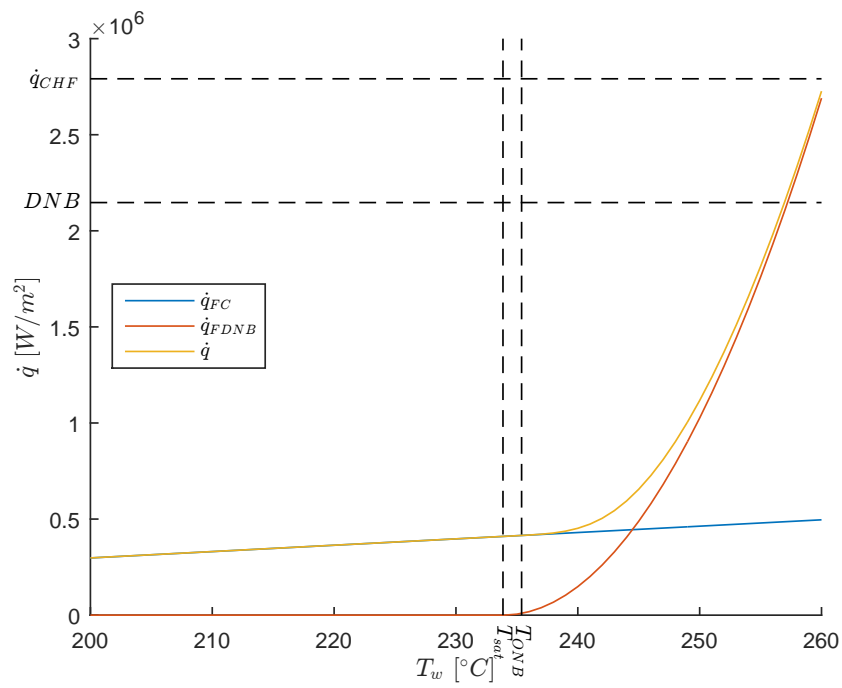


Figure 3.20: Relation between heat flux and wall temperature for mass flow rate $\dot{m}_{total} = 1 \text{ kg/s}$. Blue is forced convection heat flux \dot{q}_{FC} , red is fully developed nucleate boiling heat flux \dot{q}_{FDNB} and yellow is unifying expression \dot{q} . For large wall superheat the heat flux exceeds DNB limit.

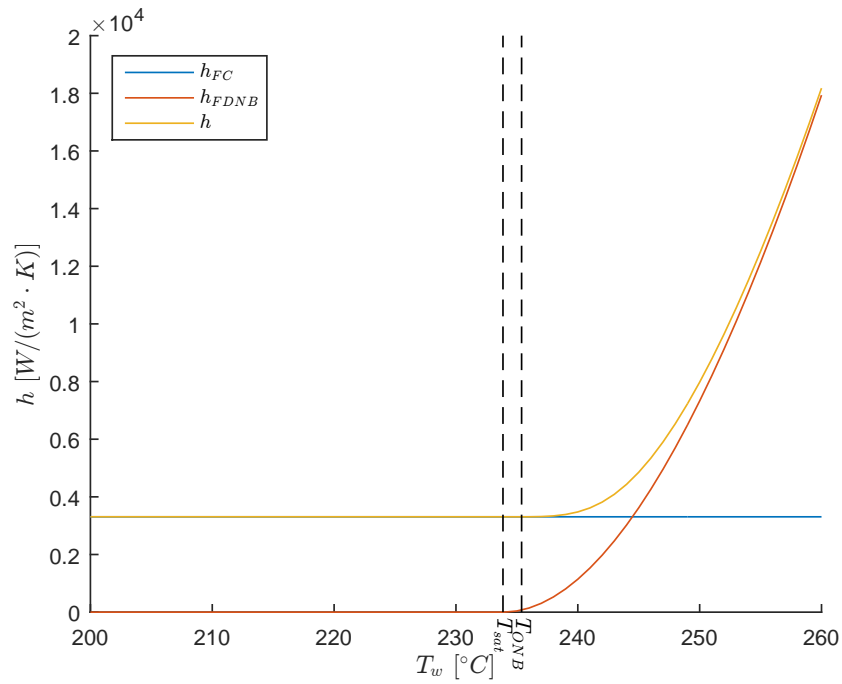


Figure 3.21: Relation between convective heat flux coefficient and wall temperature for mass flow rate $\dot{m}_{total} = 1 \text{ kg/s}$. Blue is forced convection heat transfer coefficient \dot{h}_{FC} , red is fully developed nucleate boiling heat transfer coefficient \dot{h}_{FDNB} and yellow is uniting expression \dot{h} .

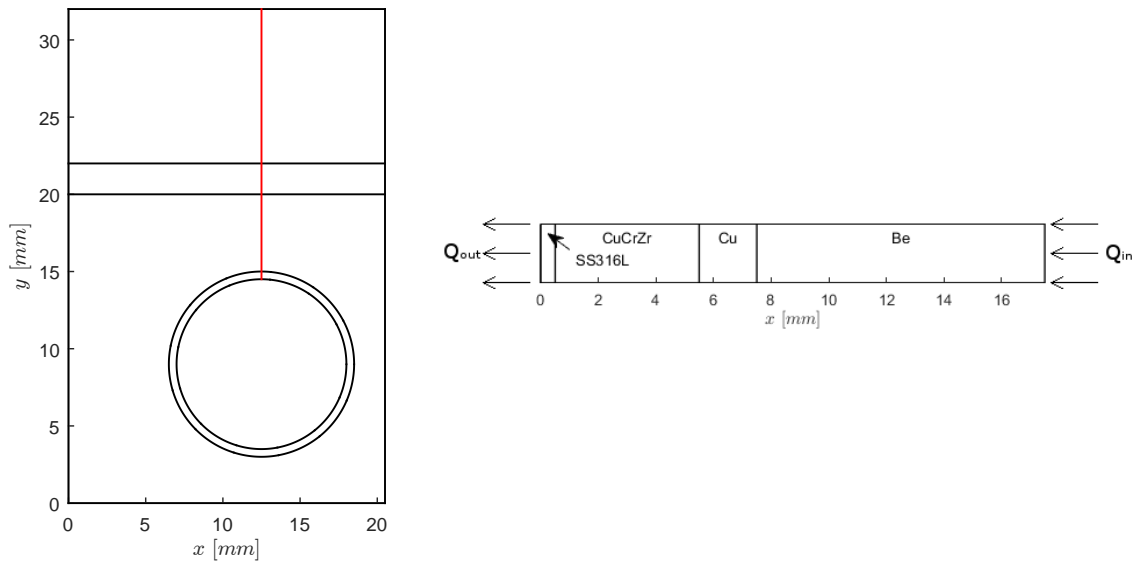


Figure 3.22: Diagram of 1D model setup. On the left, the location of 1D line in cross-sectional view of the finger. On the right, the diagram of 1D line materials and boundary conditions.

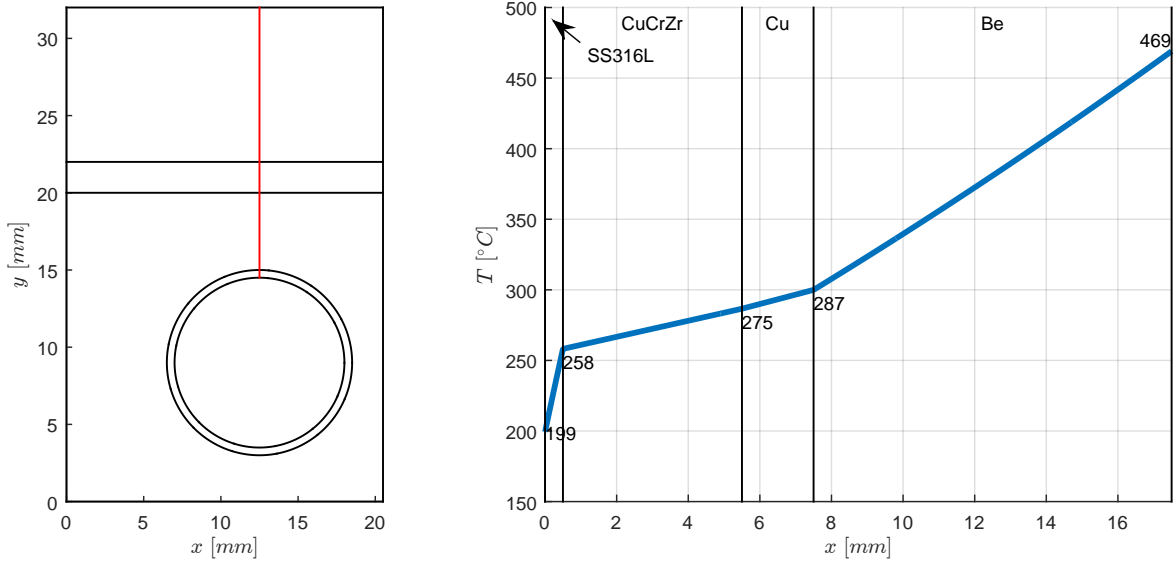


Figure 3.23: 1D example - line graph of temperature T [$^{\circ}\text{C}$] for the heat flux $\dot{q} = 2 \text{ MW}/\text{m}^2$ and for mass flow rate $10 \text{ kg}/\text{s}$. On the left is in red depicted the position of the line.

In steady-state, the heat flux at the tube wall is same as the heat flux on beryllium, and the wall temperature T_w can be evaluated by solving equation (2.52). Using the thermal resistance approach the temperature distribution can be calculated. But because thermal conductivities of materials are temperature dependent, it is not possible to reduce a material to a single thermal resistor.

Instead, the line was divided to 176 segments of length of $dx = 0.1 \text{ mm}$ and they were treated as separate thermal resistors. The temperature $T(x)$ is function of position x . The temperature at the tube side is an initial condition, $T(x = 0) = T_w$. The next temperatures are calculated recursively using equation (2.23) with an expression adjusting for spatially and temperature variant thermal conductivity $k(x, T)$:

$$T_{i+1} = \frac{\dot{q}}{\frac{|k(x_{i+1}, T_{i+1}) + k(x_i, T_i)|}{2}} dx + T_i, \quad (3.9)$$

where T_i , x_i are temperature and position at $x = i \cdot dx$.

Because the thermal conductivity depends on temperature, the equation (3.9) must be solved iteratively for each segment.

This procedure was implemented in Mathworks Matlab and a resulting temperature distribution for the heat flux $\dot{q} = 2 \text{ MW}/\text{m}^2$ and for mass flow rate $10 \text{ kg}/\text{s}$ can be seen in the fig. 3.23. It is worth noticing, how lower thermal conductivity of a material results in sharper incline in the temperature data.

In 1D model, the heat flux through the tube is equal to the heat flux applied to the beryllium and by comparing this to the critical heat flux, the departure from nucleate boiling can be predicted.

3.4 2D model

The next step was a 2D model in a plane perpendicular to the cooling tube located at the end of the finger, where the mean water temperature is $T_m = T_e = 110\text{ }^\circ\text{C}$. This problem can be described as a two-dimensional, steady-state heat conduction with following boundary conditions: constant heat flux at the beryllium surface, convection boundary at the tube surface and insulation at the rest of open surfaces.

The local heat transfer coefficient h depends on the local wall temperature T_w and so the temperature distribution must be evaluated iteratively. I used the computing software *COMSOL* with its implemented feature for solving heat transfer problems.

COMSOL offers 9 settings for the mesh density. The finest, normal and the coarsest meshes are shown in the fig. 3.24. Three parameters were selected for mesh convergence study - maximal temperature T_{max} , average temperature T_{avg} and minimal temperature T_{min} . The change in these parameters with increasing mesh density is illustrated in figures A.1, A.2 and A.3. It was decided that the use of normal mesh provides acceptable accuracy.

The figure 3.25 shows the temperature distribution for heat flux 2 MW/m^2 and for mass flow rate 10 kg/s . It goes without saying that the 2D model provides more information than the 1D model. Firstly, the hottest spot is located in the top left corner, so the 1D model could not capture it. Secondly, the tube itself has significant effect on the temperature distribution.

Temperature gradient depicted in the fig. 3.26 shows how low thermal conductivity of material is correlated with large temperature gradients. Moreover, in the CuCrZr layer you can see that the lines of constant gradient are normal to the borders. This is a result of the insulation boundary condition.

The figure 3.27 represents the rise of temperature from the CuCrZr layer to the beryllium on the outer edge of the finger. The highest value is also the maximum temperature for the whole cross-section.

The figure 3.28 illustrates the wall temperature of the tube. The slight asymmetry in the positioning of the tube causes the peak value to be located at the angle greater than 180° . It is pointing towards the top left corner, which is the point with heat flux applied to it farthest away from the center of the tube. The maximum wall temperature in this case reaches $188\text{ }^\circ\text{C}$. Because it does not exceed the saturation temperature of $233\text{ }^\circ\text{C}$, there is no boiling and the heat transfer at the wall-coolant interface is only by forced convection.

Knowing the wall temperature T_w , the local convective heat transfer coefficient h_w then can be calculated for every point at the tube-water interface using the equation (2.53). Subsequently, the local heat flux at the wall \dot{q}_w can be estimated as

$$\dot{q}_w = h(T_w)(T_w - T_e), \quad (3.10)$$

where T_m is the mean temperature of water at the outlet, which is $110\text{ }^\circ\text{C}$.

To avoid the occurrence of departure from nucleate boiling, this local heat flux is compared to critical heat flux to discover unacceptable operation parameters.

3.5 3D model

The constant heat flux to the beryllium causes the mean temperature of water to rise linearly from the inlet to the outlet. Coupled with the simplified geometry of the model, where cross-section perpendicular to the tube is constant all along the tube, my hypothesis was that the 3D

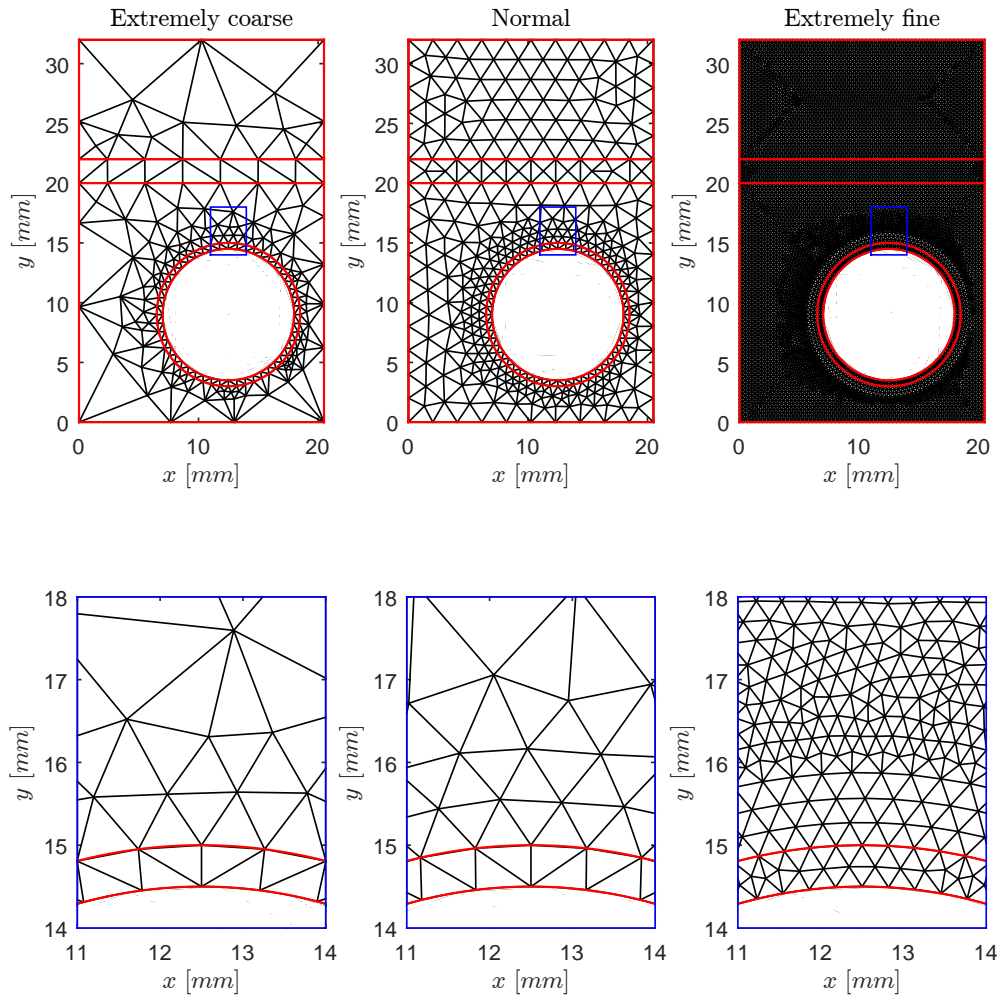


Figure 3.24: Example of several meshes with the finger structure highlighted in red and detailed views of the area in the blue rectangle, which shows mesh near the tube-coolant interface.

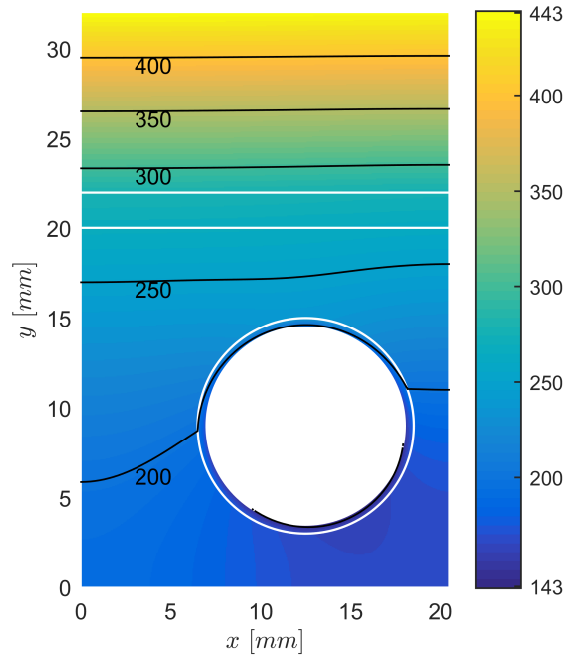


Figure 3.25: 2D model - temperature distribution T [$^{\circ}C$] for the heat flux $\dot{q} = 2 \text{ MW}/m^2$ and for mass flow rate $\dot{m}_{total} = 10 \text{ kg}/s$. The structure of the finger is marked in white.

model will not bring much more new information than the 2D model. To test this hypothesis, the 2D and 3D model were compared for the heat flux $2 \text{ MW}/m^2$ and for mass flow rate $\dot{m}_{total} = 10 \text{ kg}/s$.

The fig. 3.29 represents temperature distribution on a channel of length of 377.6 mm heated with uniform heat flux $2 \text{ MW}/m^2$ and cooled by water with mass flow rate of $10 \text{ kg}/s$ and mean temperature linearly rising from $70 \text{ }^{\circ}C$ at the inlet to $110 \text{ }^{\circ}C$ at the outlet.

To better illustrate the development of temperatures in each material along the tube, the fig. 3.30 shows dependency of maximum temperatures of every material on the position along the tube. From the graph it is clear that the linear trend and an overall increase of about $40 \text{ }^{\circ}C$ from the inlet to the outlet is roughly transmitted to all of the materials. This outcome supports the hypothesis that the 3D model does not provide additional information.

To further investigate the necessity of the 3D model, the results from 2D and 3D model were directly compared. A 2D cut at the outlet level was made from the 3D data as this is the exact same situation the 2D model was trying to simulate (see fig. 3.31). This comparison is shown in the fig. 3.32. The maximum temperature difference is roughly $2 \text{ }^{\circ}C$, or about 1% . Considering the geometry simplifications and generally imprecise nature of empirical correlations in estimating of the heat transfer coefficient, this error is acceptable as it will not significantly affect results.

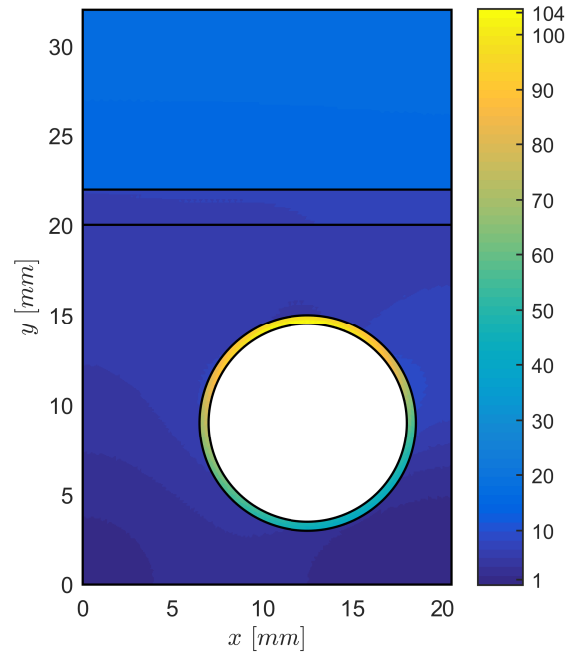


Figure 3.26: 2D model - absolute value of temperature gradient in $[\text{°C}/\text{mm}]$ for the heat flux $\dot{q} = 2 \text{ MW}/\text{m}^2$ and for mass flow rate $\dot{m}_{total} = 10 \text{ kg}/\text{s}$. The structure of the finger is marked in black. It is clear that different thermal conductivity effects the gradient. The difference between beryllium and copper is apparent. The highest temperature gradient is in the tube as SS316L has low conductivity.

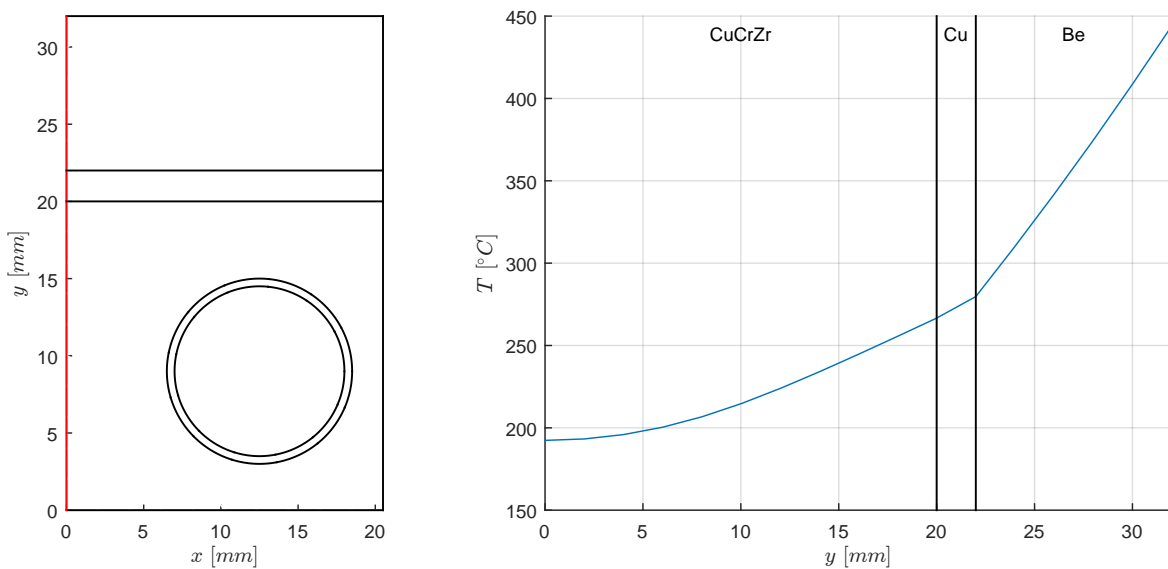


Figure 3.27: 2D model - line graph of temperature T $[\text{°C}]$ along the outer edge of the finger for the heat flux $\dot{q} = 2 \text{ MW}/\text{m}^2$ and for mass flow rate $\dot{m}_{total} = 10 \text{ kg}/\text{s}$. On the left is in red depicted the position of the line.

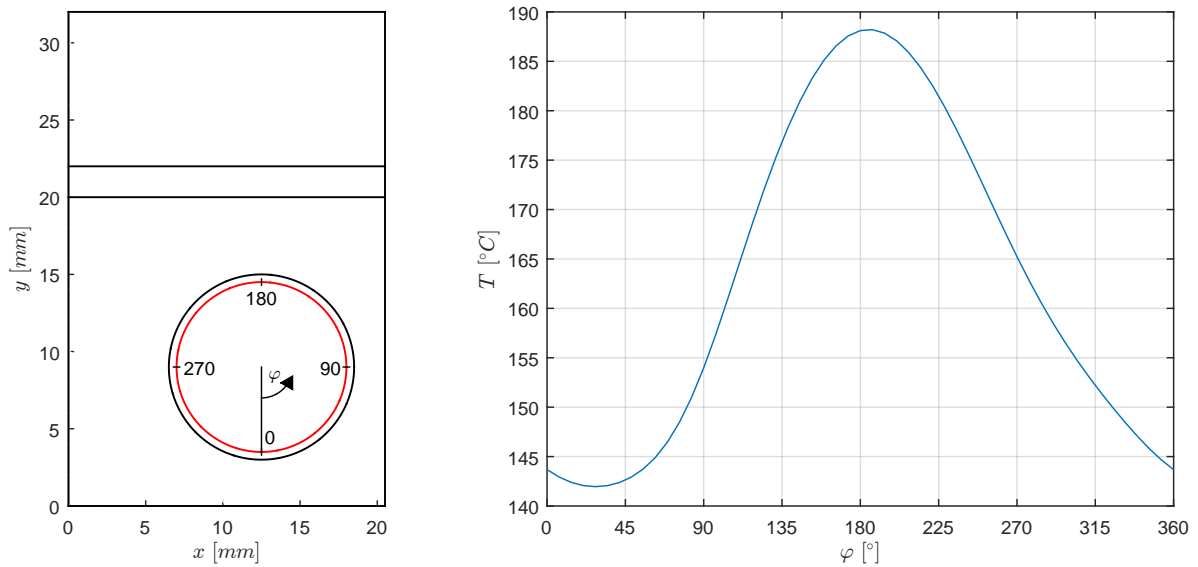


Figure 3.28: 2D model - line graph of temperature T [$^{\circ}C$] along the tube surface for the heat flux $\dot{q} = 2 \text{ MW}/m^2$ and for mass flow rate $\dot{m}_{total} = 10 \text{ kg}/s$. On the left is in red depicted the position of the tube surface and the values of angle φ .

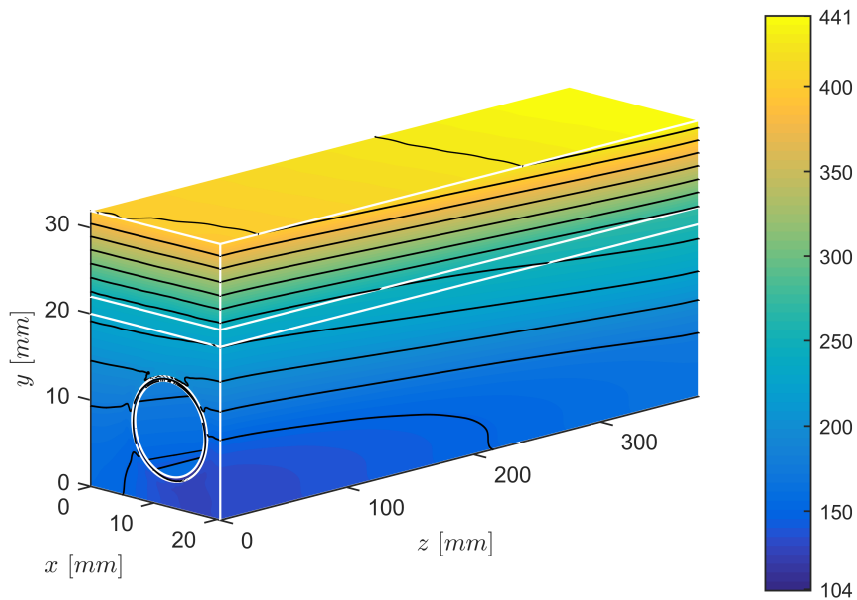


Figure 3.29: 3D example - temperature distribution T [$^{\circ}C$] for the heat flux $2 \text{ MW}/m^2$ and for mass flow rate $\dot{m}_{total} = 10 \text{ kg}/s$. Flow of the coolant is in the direction of z axis. The black lines represent surfaces of same temperature. The structure of the finger is marked in white.

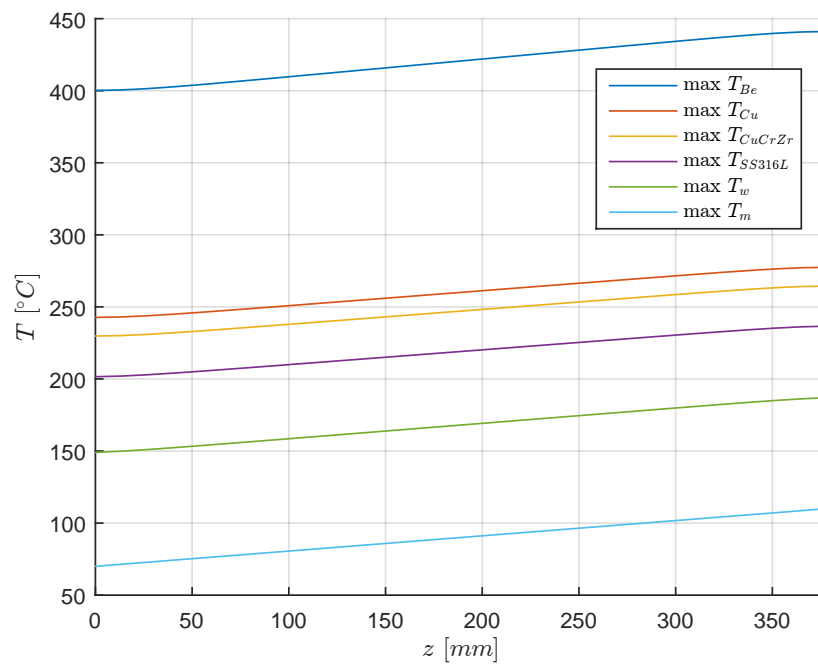


Figure 3.30: 3D example - max. temperatures of different materials (beryllium, copper, CuCrZr, SS316L, wall of the SS316L tube, mean temperature of water) along the tube for the heat flux $2 \text{ MW}/\text{m}^2$ and for mass flow rate $\dot{m}_{total} = 10 \text{ kg}/\text{s}$. Coolant flows in the direction of the z axis.

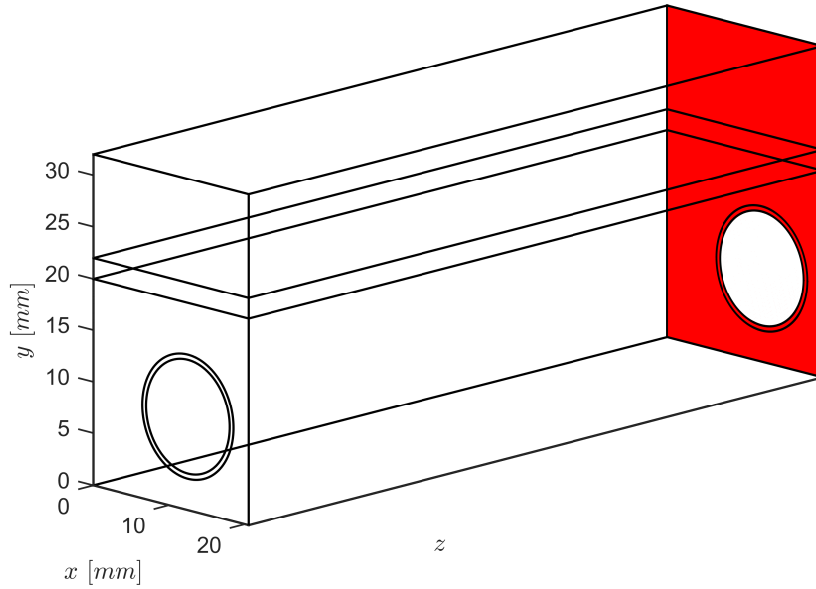


Figure 3.31: 3D model - representation of a cut-plane identical to the 2D model. Coolant flows in the direction of the z axis.

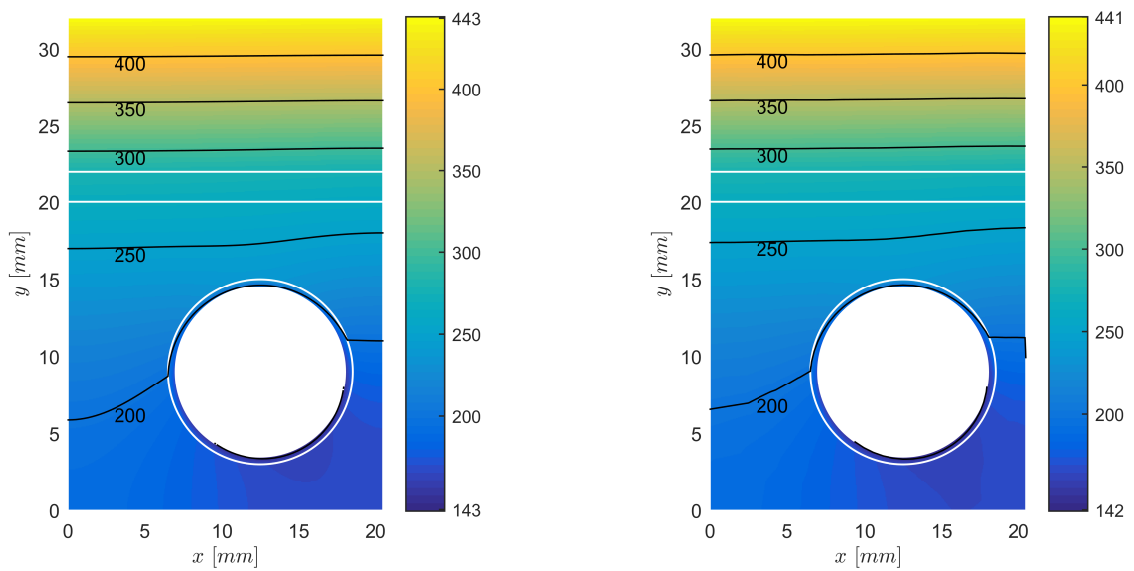


Figure 3.32: Comparison of a 2D model (left) and a cut from 3D model (right) for the heat flux 2 MW/m^2 and for mass flow rate $\dot{m}_{total} = 10 \text{ kg/s}$.

Chapter 4

Results

To investigate the effect of different heat fluxes and water mass flow rates on the finger, I have performed a parametric sweep for both 1D and 2D model. The 3D model was omitted, because it was shown that it does not bring in any new significant information. The heat flux range (0.5 – 4.7) MW/m^2 was sampled with a step of 0.1 MW/m^2 and the mass flow rate with a step of 0.2 kg/s in the range of (1 – 15) kg/s . This sampling yields a matrix 43×71 of all possible combinations of those parameters.

4.1 1D model

Each of these combinations served as an input parameter to the 1D model described previously.

First, the critical heat flux \dot{q}_{CHF} (fig. 3.19) and the heat flux \dot{q} input parameter were used to calculate the $DNBR$ defined in equation (2.44). In the fig. 4.1, the values of $DNBR$ over the parameter domain are shown. As was already mentioned, it is better to be cautious about the critical heat flux, because the impacts on system when it is reached might be quite severe. Therefore, safety margin is introduced. If the $DNBR$ is lower than 1.3, the possibility of a critical situation is too high. The acceptable parameters from $DNBR$ analysis are presented in the fig. 4.2.

Subsequently, the 1D model described on the page 33 was used to calculate the temperature distribution for every set of input parameters \dot{q} and \dot{m}_{total} .

The maximal wall temperature T_w is shown in the fig 4.3. We can distinguish two regions with different heat transfer mechanisms which are divided by the temperature of onset of nucleate boiling T_{ONB} (between 235.5 and 238.5 °C depending on the mass flow rate). If the wall temperature is below the T_{ONB} , the heat transfer mechanisms is only through forced convection. This region roughly corresponds to the blue area in the fig. 4.3. The yellow area, where $T_w > T_{ONB}$, is dominated by nucleate boiling. The enhanced heat transfer of this mechanism translates into the small increments in wall temperature needed to accommodate for bigger heat transfer \dot{q} .

The maximum temperatures in SS316L, CuCrZr and copper layers are depicted in figures A.4, A.5, resp. A.6 in the appendix.

The 1D model predicts that the top layer of beryllium will reach maximum temperatures shown in the fig. 4.4. The applied heat flux \dot{q} is obviously the more important factor from the two input parameters. We see that the increased velocity of the coolant in the tubes only marginally affects the final beryllium temperature and the influence diminishes even more in

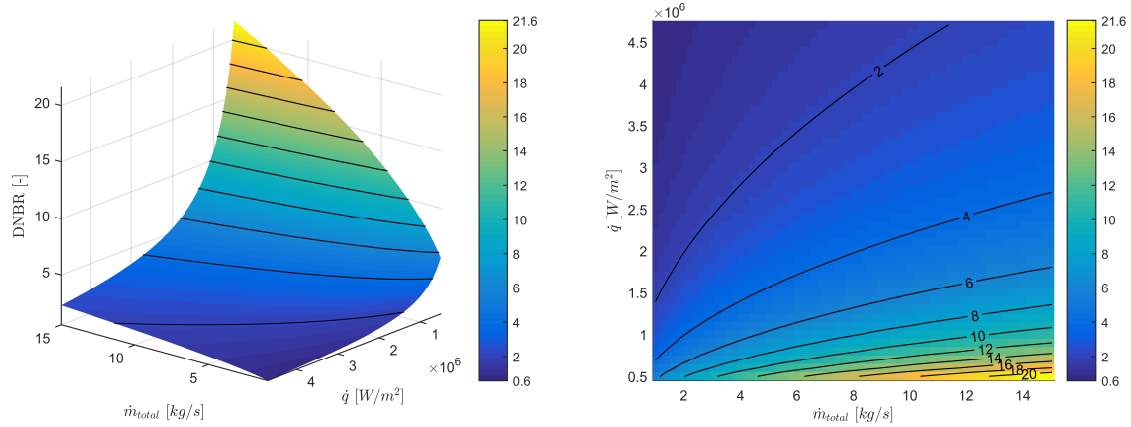


Figure 4.1: 1D model - Departure from nucleate boiling ratio $DNBR$ for combinations of heat flux \dot{q} and mass flow rate \dot{m}_{total} parameters. On the left is a 3D view, on the right, a top view with labeled counter lines.

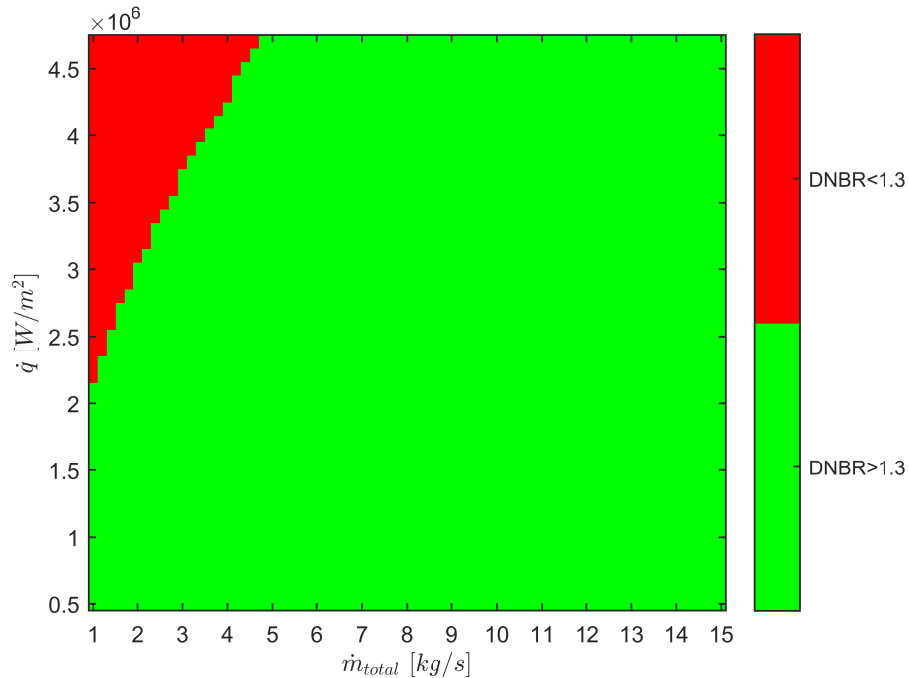


Figure 4.2: 1D model - Acceptable combinations of heat flux \dot{q} and mass flow rate \dot{m}_{total} parameters where $DNBR > 1.3$.

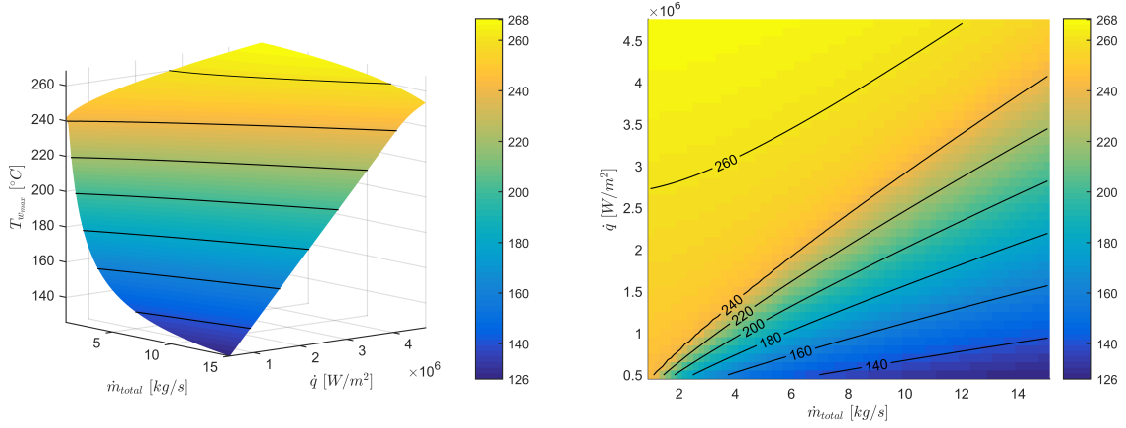


Figure 4.3: 1D model - Max. wall temperature T_w for combinations of heat flux \dot{q} and mass flow rate \dot{m}_{total} parameters. On the left is a 3D view, on the right, a top view with labeled counter lines.

high heat fluxes or with high mass flow rates.

The limit on the maximum allowable beryllium temperature is $500\text{ }^{\circ}\text{C}$. In the fig. 4.5, we see that this limit restricts large number of parameters. Most notably, all heat fluxes above $2.5\text{ MW}/\text{m}^2$ are forbidden no matter what is the water mass flow rate. Moreover, the limitations imposed by the *DNBR* are milder than those arising from the max. beryllium temperature, so the 4.5 is the final chart of parameters under which the machine can safely operate derived from the 1D model.

4.2 2D model

Using the 2D model described on page 38, the temperature distribution in the cross-sectional view was obtained for every set of input parameters \dot{q} and \dot{m}_{total} .

The maximal wall temperature T_w is shown in the fig 4.6. As in the 1D model, there is clear difference between the regions dominated by forced convection and by the nucleate boiling. The maximum temperatures in SS316L, CuCrZr and copper layers are depicted in figures A.7, A.8, resp. A.9 in the appendix. Finally, the maximum beryllium temperature is illustrated in the fig. 4.7. Again, by comparing the beryllium temperatures to the $500\text{ }^{\circ}\text{C}$ limit, we can show, which parameters are safe in the fig. 4.8.

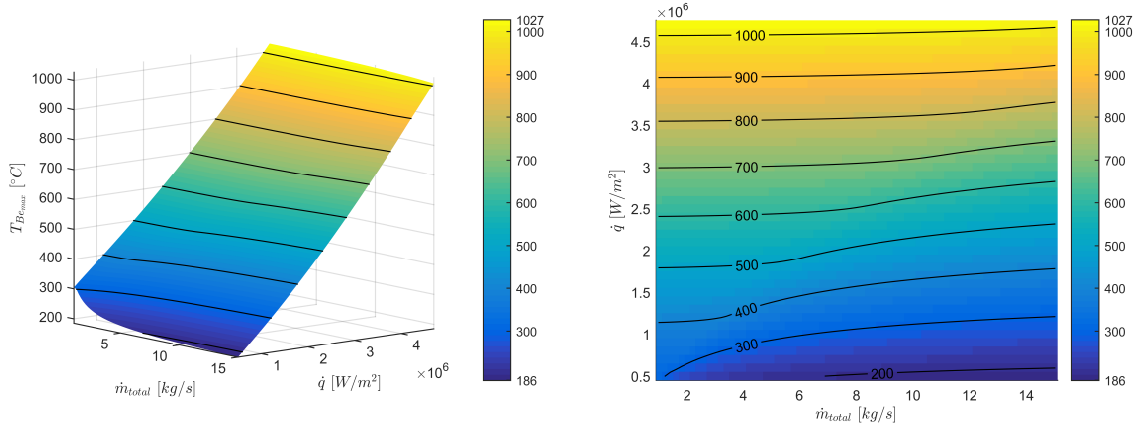


Figure 4.4: 1D model - Max. Beryllium temperature T_{Be} for combinations of heat flux \dot{q} and mass flow rate \dot{m}_{total} parameters. On the left is a 3D view, on the right, a top view with labeled counter lines.

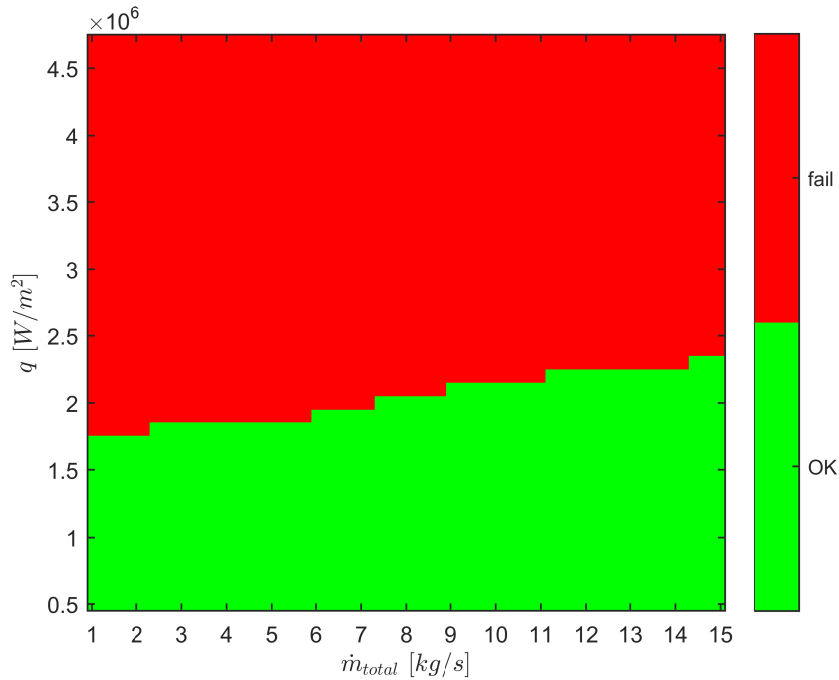


Figure 4.5: 1D model - Acceptable combinations of heat flux \dot{q} and mass flow rate \dot{m}_{total} parameters for $T_{Be} < 500$ °C.

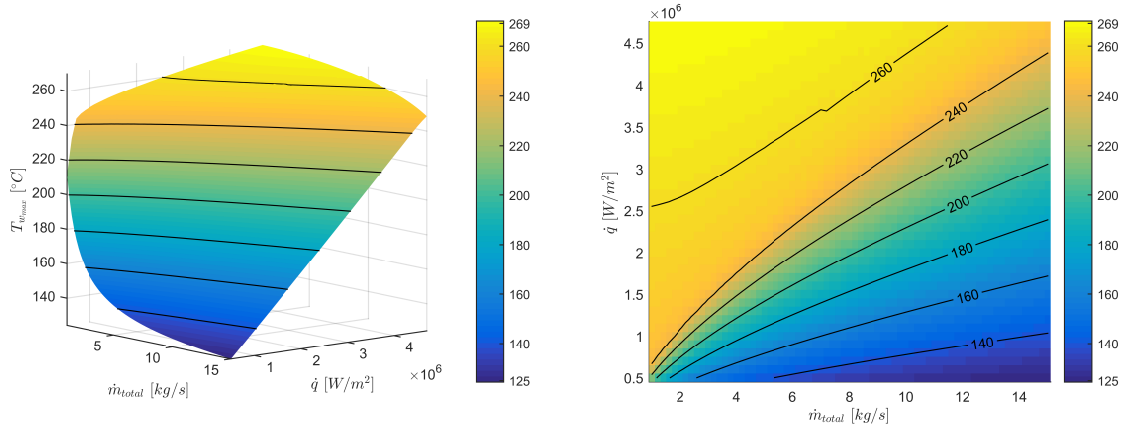


Figure 4.6: 2D model - Max. wall temperature T_w for combinations of heat flux \dot{q} and mass flow rate \dot{m}_{total} parameters. On the left is a 3D view, on the right, a top view with labeled counter lines.

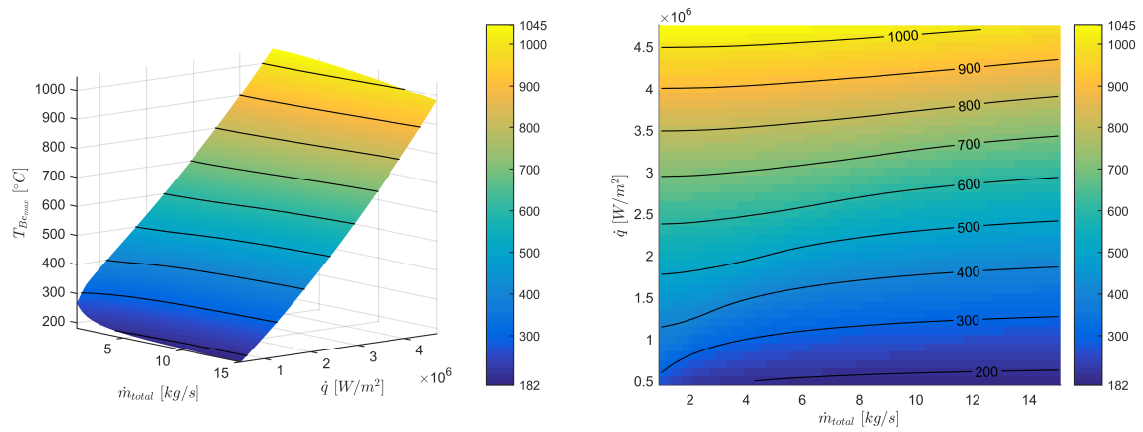


Figure 4.7: 2D model - Max. Beryllium temperature T_{Be} for combinations of heat flux \dot{q} and mass flow rate \dot{m}_{total} parameters. On the left is a 3D view, on the right, a top view with labeled counter lines.

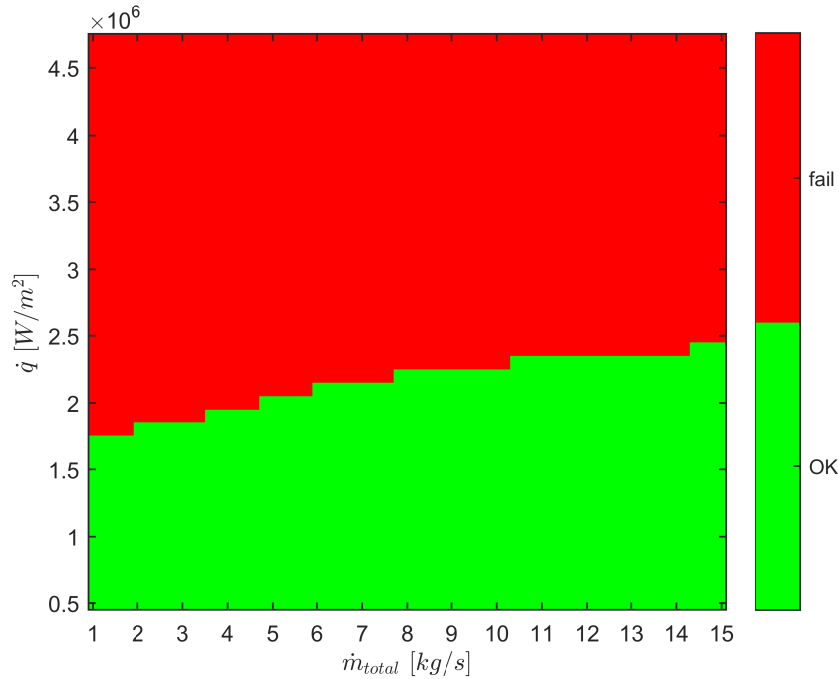


Figure 4.8: 2D model - Acceptable combinations of heat flux \dot{q} and mass flow rate \dot{m}_{total} parameters for $T_{Be} < 500 \text{ }^\circ\text{C}$.

As was discussed in the section 3.4 describing the 2D model, it is necessary to know the maximum wall temperature and from it calculated maximal local wall heat flux $\dot{q}_{w_{max}}$ to investigate the possibility of departure from the nucleate boiling. As you will see from the fig. 4.9, which shows the maximal local wall heat flux $\dot{q}_{w_{max}}$, the $\dot{q}_{w_{max}}$ can be both lower and higher than the applied heat flux \dot{q} . For example, for heat flux $\dot{q} = 4 \text{ MW/m}^2$ the wall heat flux is higher for low mass flow rates up to approx. 10 kg/s , while it is lower for the mass flow rates in the range $10 - 15 \text{ kg/s}$.

The $DNBR$ is shown in the fig. 4.10 and from it arising limitations are illustrated in the fig. 4.11.

And once again, the requirement on the maximal beryllium temperature is stronger than the limitations from critical heat flux \dot{q}_{CHF} , so the fig. 4.8 shows the final set of allowable parameters determined from the 2D model.

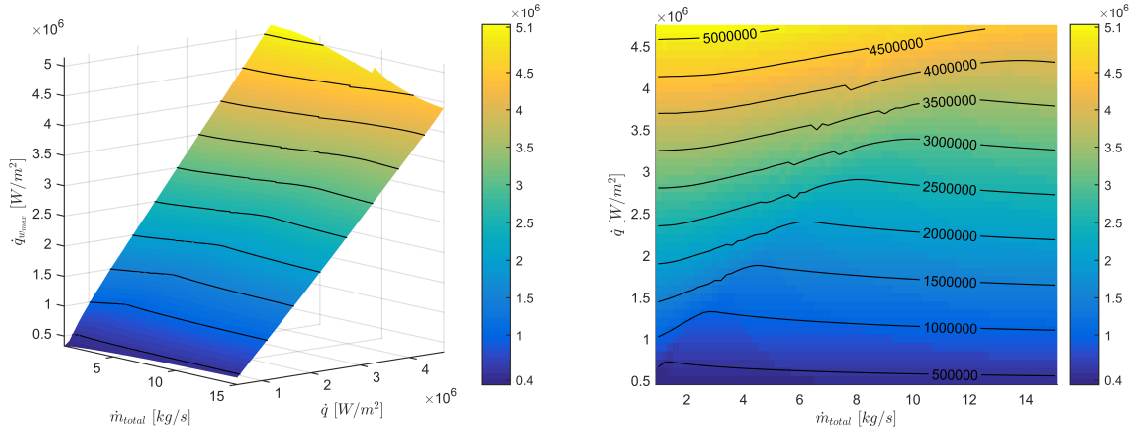


Figure 4.9: 2D model - Max. local wall heat flux $\dot{q}_{w,max}$ for combinations of heat flux \dot{q} and mass flow rate \dot{m}_{total} parameters. On the left is a 3D view, on the right, a top view with labeled counter lines.

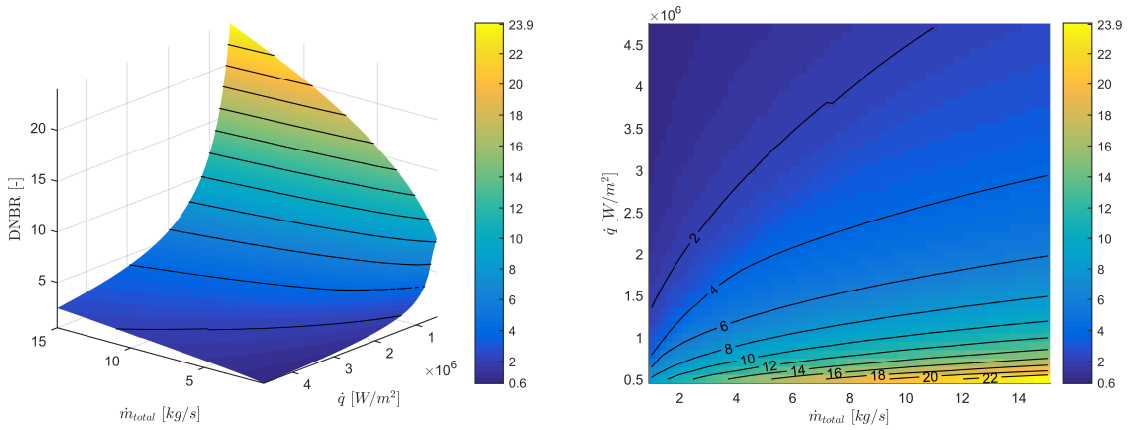


Figure 4.10: 2D model - Departure from nucleate boiling ratio $DNBR$ for combinations of heat flux \dot{q} and mass flow rate \dot{m}_{total} parameters. On the left is a 3D view, on the right, a top view with labeled counter lines.

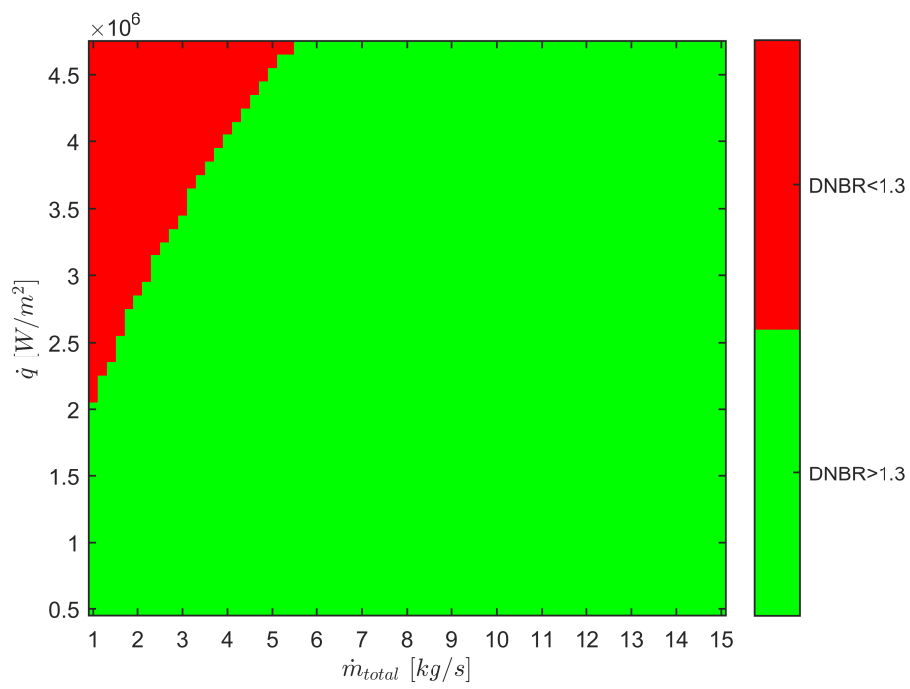


Figure 4.11: 2D model - Acceptable combinations of heat flux \dot{q} and mass flow rate \dot{m}_{total} parameters where $DNBR > 1.3$.

Discussion and Conclusion

My task was to investigate the effect of combinations of heat flux and cooling water mass flow rate on the temperatures of ITER FW panels that will be tested in *HELICZA* device. To guarantee, safety of this testing device two limits were set: one for the water temperature at the outlet and maximum allowable temperature for beryllium, which is the plasma facing material on the ITER FW panels.

I constructed an simplified model of the panel and created 1D, 2D and 3D models for studying the heat transfer through the panel. I showed that the 3D model is not necessary since it does not provide significant new information. The 1D model was used as an reference and validation for the more complicated 2D model. It is important to note that the model has its limitations: the simplified geometry, steady-state heat transfer or experimental correlations for evaluating the heat transfer coefficient. I tried to make the simplifications and assumptions conservative, so the model rather overestimates the situation.

The fig. 4.8 shows final set of acceptable parameters for safe operation of *HELICZA*. We see that all heat fluxes above 2.5 MW/m^2 are restricted. This is not an issue, since FW06A panel is a normal heat flux panel designed for heat loads up to 2 MW/m^2 . Interesting is that increased water mass flow rate does only marginally improves heat transfer. The reason is that when boiling occurs in the tube and the heat transfer mechanism changes to nucleate boiling, the majority of heat is extracted by evaporation of the water and the influence of the flow velocity on the heat transfer is very diminished.

R. Zanino et al. had performed similar thermal analysis of the FW06A panel in their articles *CFD analysis of the ITER first wall 06 panel. Part I: Model set-up and flow distribution* [23] and *CFD analysis of the ITER first wall 06 panel. Part II: Thermal-hydraulics* [24]. They used complete 3D model of a single hydraulic channel for the analysis. The cooling water had inlet temperature $70 \text{ }^\circ\text{C}$, pressure was 4 MPa and mass flow rate 5.3 kg/s . The panel was heated by both nuclear volumetric and plasma surface loads. Since the nuclear volumetric load was 0.37 MW and the plasma surface heat load was combination of 0.35 MW/m^2 and toroidally shaped heat load profile from 0 to 2 MW/m^2 , comparison with my results is difficult. For these parameters, they have reached outlet water temperature $127.2 \text{ }^\circ\text{C}$ (over limit we want to comply with), maximum wall temperature $228.5 \text{ }^\circ\text{C}$ and maximum beryllium temperature $492.7 \text{ }^\circ\text{C}$.

If we assume in our 2D model heat flux $\dot{q} = 2 \text{ MW/m}^2$ and mass flow rate $\dot{m}_{total} = 5.3 \text{ kg/s}$, we get approximately maximum wall temperature $240 \text{ }^\circ\text{C}$ and maximum beryllium temperature $500 \text{ }^\circ\text{C}$. Although, this comparison is very imprecise because of the different input parameters, it shows that my 2D model is in rough agreement with the results of Zanino et al.

4.3 Conclusion

I have developed model of cooling system of ITER FW panel that will be tested in *HELICZA* device. I used this model to analyze the steady-state heat transfer through this panel for given range of electron beam effective heat flux densities and for water coolant mass flow rate through the panels. Comparing the results of my model with limits on beryllium temperature and the outlet water temperature, I was able to determine which combinations of those parameters should be safe for operation. The suitable parameters are represented in the fig. 4.12. However, under the assumption of uniform heat flux, the irradiated area of a hydraulic channel must be less than the percentage of total hydraulic channel area given by the fig. 4.13.

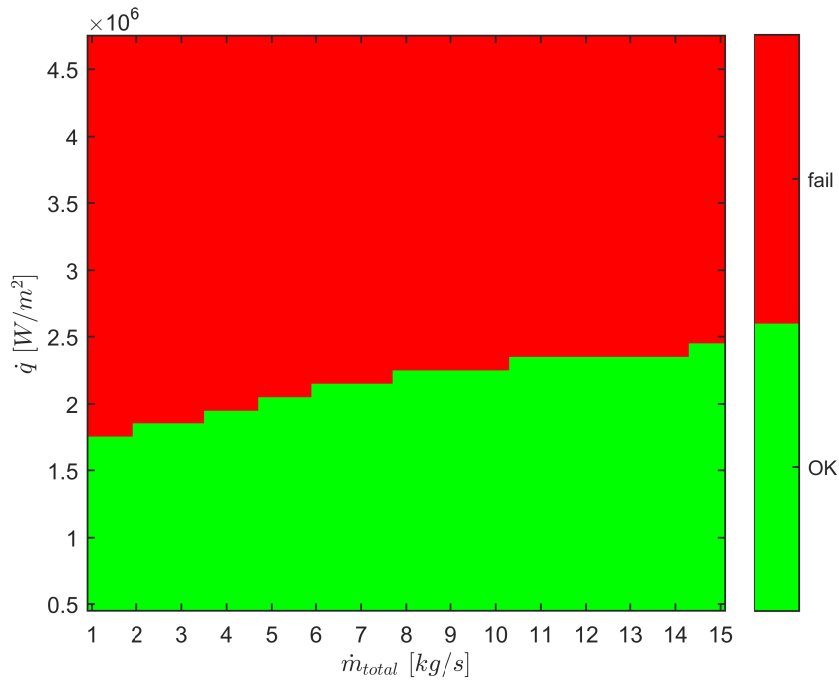


Figure 4.12: Acceptable combinations of heat flux \dot{q} and mass flow rate \dot{m}_{total} parameters for operation of the testing device *HELICZA*.

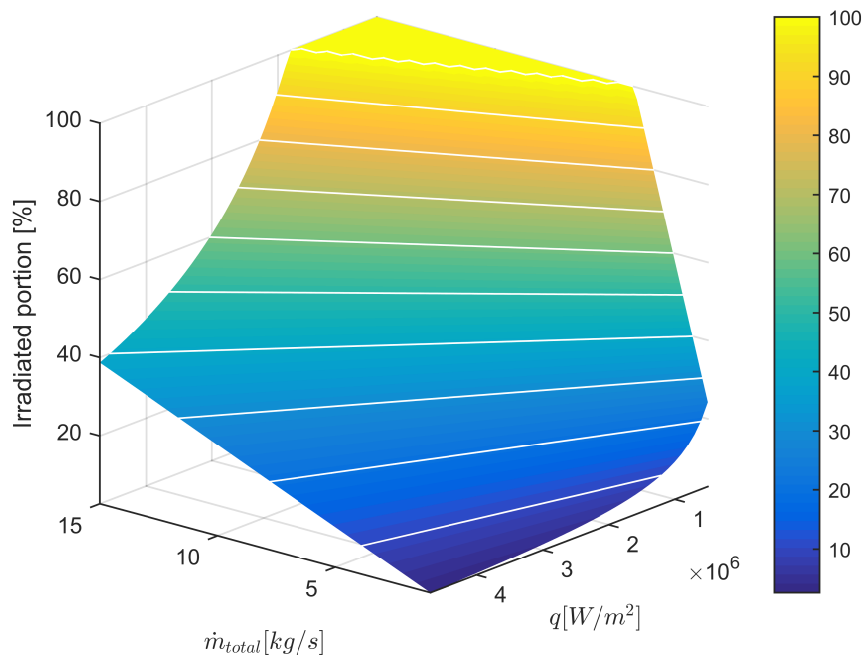


Figure 4.13: Maximum allowable percentage of the area of hydraulic channel to be irradiated.

Appendix A

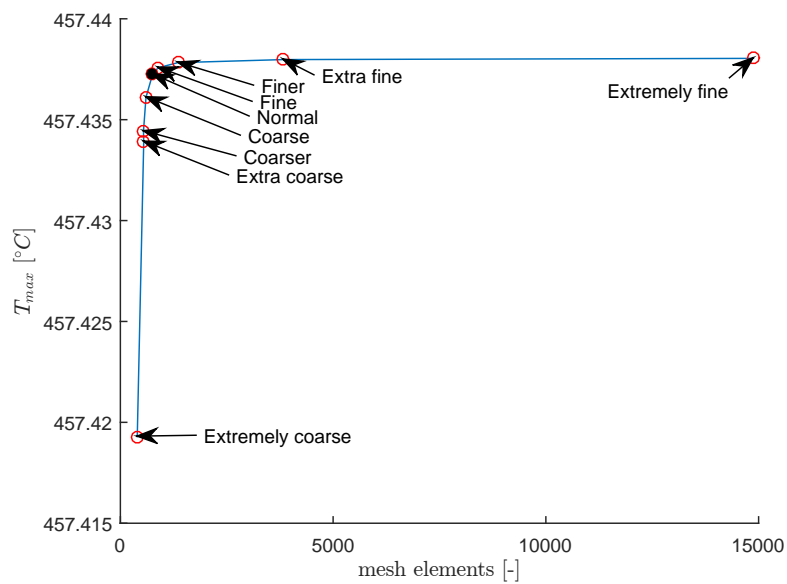


Figure A.1: Maximum finger temperature T_{max} dependency on number of mesh elements. The labeled data points represent different mesh densities. The black filled data point is normal setting, which was then used in following calculations.

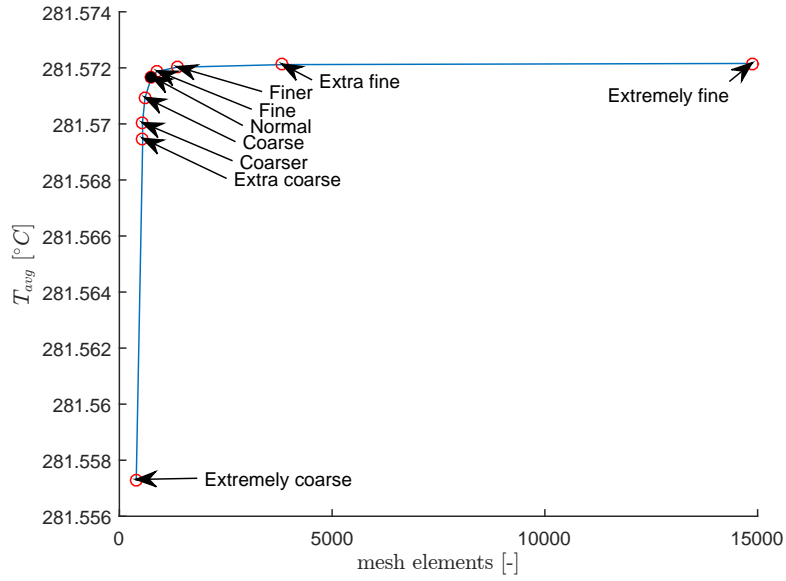


Figure A.2: Average finger temperature T_{avg} dependency on number of mesh elements. The labeled data points represent different mesh densities. The black filled data point is normal setting, which was then used in following calculations.

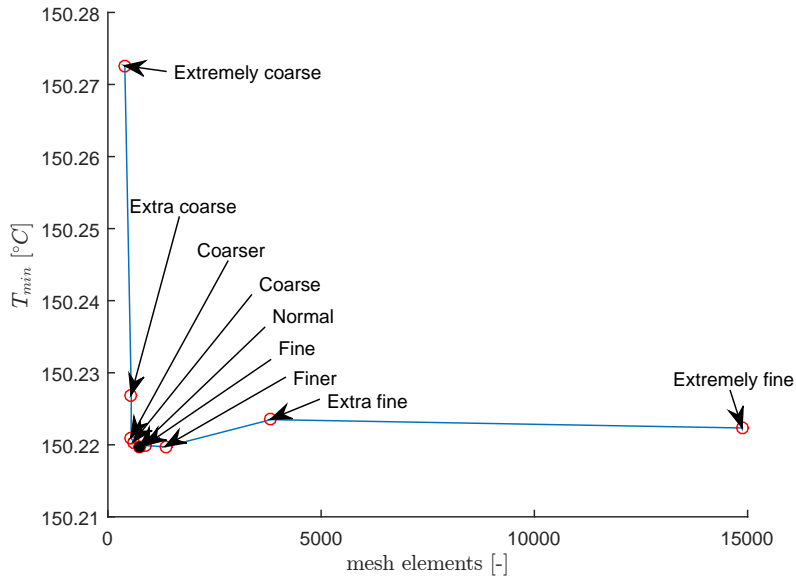


Figure A.3: Minimum finger temperature T_{min} dependency on number of mesh elements. The labeled data points represent different mesh densities. The black filled data point is normal setting, which was then used in following calculations.

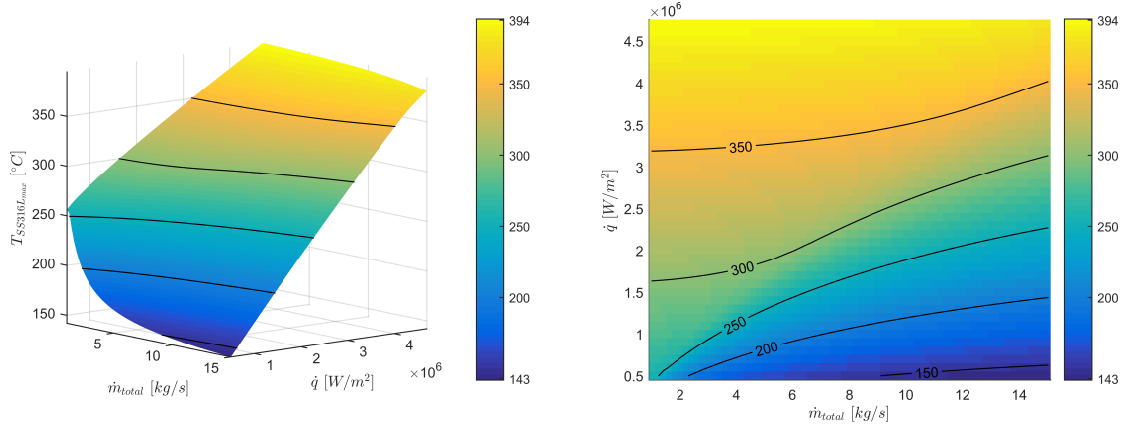


Figure A.4: 1D model - Max. SS316L temperature T_{SS316L} for combinations of heat flux \dot{q} and mass flow rate \dot{m}_{total} parameters. On the left is a 3D view, on the right, a top view with labeled counter lines.

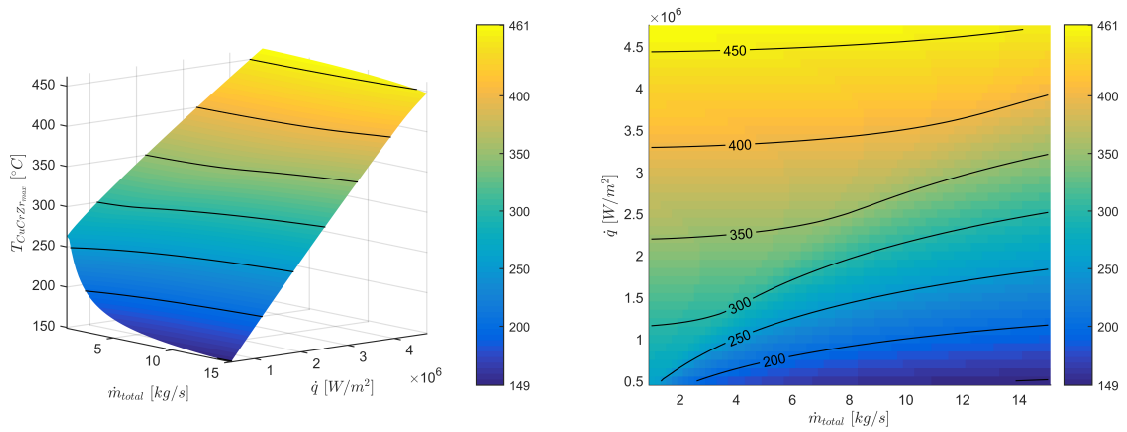


Figure A.5: 1D model - Max. CuCrZr temperature T_{CuCrZr} for combinations of heat flux \dot{q} and mass flow rate \dot{m}_{total} parameters. On the left is a 3D view, on the right, a top view with labeled counter lines.

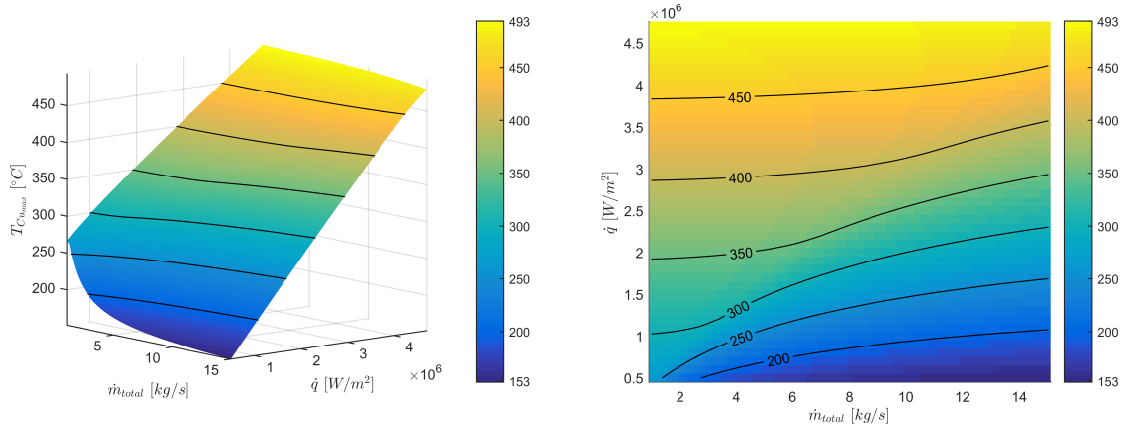


Figure A.6: 1D model - Max. Cu temperature T_{Cu} for combinations of heat flux \dot{q} and mass flow rate \dot{m}_{total} parameters. On the left is a 3D view, on the right, a top view with labeled counter lines.

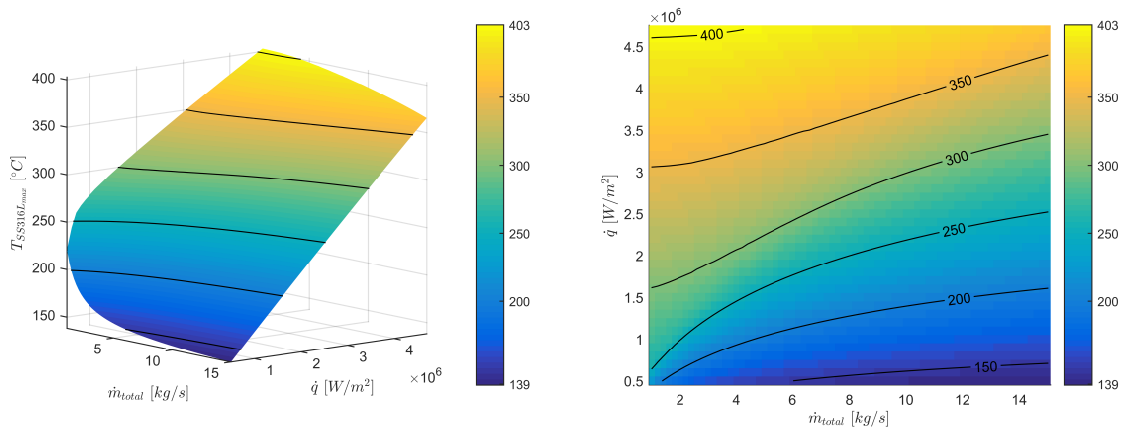


Figure A.7: 2D model - Max. SS316L temperature T_{SS316L} for combinations of heat flux \dot{q} and mass flow rate \dot{m}_{total} parameters. On the left is a 3D view, on the right, a top view with labeled counter lines.

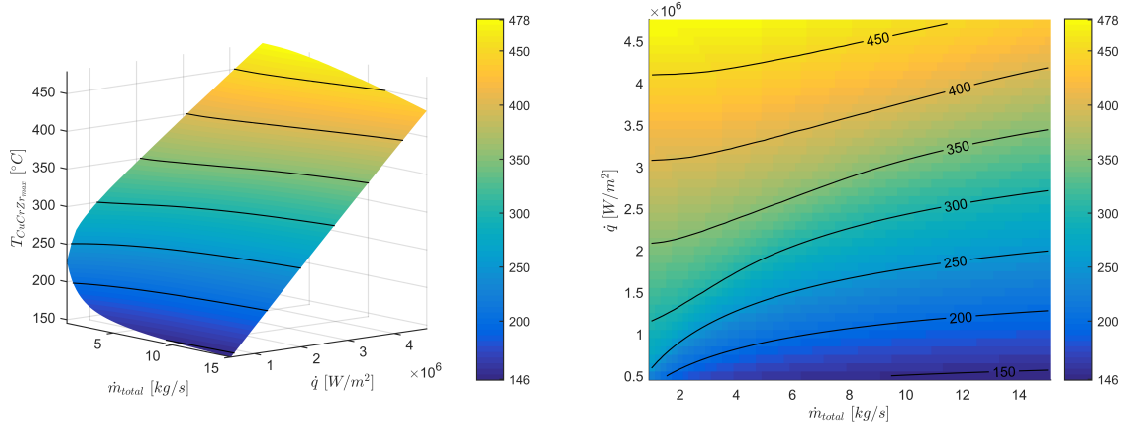


Figure A.8: 2D model - Max. CuCrZr temperature T_{CuCrZr} for combinations of heat flux \dot{q} and mass flow rate \dot{m}_{total} parameters. On the left is a 3D view, on the right, a top view with labeled counter lines.

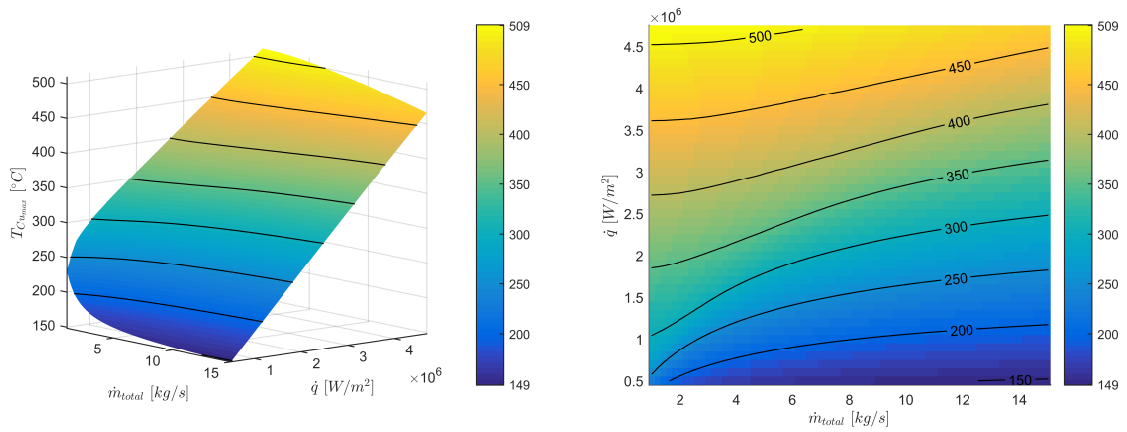


Figure A.9: 2D model - Max. Cu temperature T_{Cu} for combinations of heat flux \dot{q} and mass flow rate \dot{m}_{total} parameters. On the left is a 3D view, on the right, a top view with labeled counter lines.

Bibliography

- [1] A. E. Bergles and W. M. Rohsenow. The determination of forced convection surface boiling heat transfer. *J. Heat Transfer (86)*: 365–372, 1964.
- [2] Y. A. Çengel and A. J. Ghajar. *Heat and Mass Transfer: Fundamentals and Applications 5th edition*. McGraw-Hill Education, New York, N.Y., 2015.
- [3] G.P. Celata, M. Cumo, and A. Mariani. Assessment of correlations and models for the prediction of CHF in water subcooled flow boiling. *International Journal of Heat and Mass Transfer*, 37(2):237 – 255, 1994.
- [4] T. Cicero, M. Jimenez, Gabriele D’Amico, Jordi Ayneto Pou, Georges Dellopoulos, Elena Alvaro, Sabas Cardenes, Stefano Banetta, Boris Bellin, Francesco Zacchia, Barbara Calcagno, Philippe Chappuis, Stefan Gicquel, Raphael Mitteau, and Rene Raffray. Progress in the design of normal heat flux first wall panels for ITER. *Fusion Engineering and Design*, 2015.
- [5] M. L. Corradini. *Fundamentals of Multiphase Flow*. Department of Engineering Physics, University of Wisconsin, 1997. Retrieved from <http://wins.engr.wisc.edu/teaching/mpfBook/main.html>.
- [6] P. W. Dittus and L. M. K. Boelter. Heat transfer in automobile radiators of the tubular type. *Int. Comm. Heat Mass Transfer*, (12): 3–22, 1985.
- [7] F. Romanelli et al. *Fusion Electricity – A roadmap to the realisation of fusion energy*. European Fusion Development Agreement, 2012. ISBN 978-3-00-040720-8.
- [8] S. Entler et al. *Experimental Complex HELCZA Preliminary Design, revision 1.4*. Research Centre Rez, CVR 271, May 2014.
- [9] X. Fang, R. Shi, and Z. Zhou. Correlations of flow boiling heat transfer of r-134a in minichannels: comparative study. *Energy Science and Technology*, 1(1):1–15, 2011.
- [10] Fusion for Energy. *Overview of the ITER first wall panels*. Fusion for Energy, 2009. Retrieved from http://www.iter-industry.ch/wp-content/uploads/2010/05/Overview-of-ITER-Blanket-FW_Industry-ppt.pdf.
- [11] Fusion for Energy. *Technical Specifications for High Heat Flux Test Facility for In-vessel Components and High Heat Flux Testing, F4E-OPE-319 ver.8*. Fusion for Energy, 2013.
- [12] E. Forrest, J. Buongiorno, T. McKrell, and L. Hu. Thermal Hydraulic Study of Utilizing Unfinned Plate Fuel in the MITR. 34th *International Meeting on Reduced Enrichment for Research and Test Reactors*, Warsaw, 2012.

- [13] US ITER. The ITER tokamak. http://www.iter.org/doc/all/content/com/gallery/Media/7%20-%20Technical/2009_04_29%20MACHINE.jpg.
- [14] ITER Organization. *ITER structural design criteria for in-vessel components, Appendix A, Materials design limit data*. G 74 MA 8 01-05-28 W0.2.
- [15] T. A. Fallon J. R. S. Thom, W. M. Walker and G. F. S. Reising. Boiling in subcooled water during flow up heated tubes or annuli. *Symposium on Boiling Heat Transfer in Steam Generation Units and Heat Exchangers, Manchester, IMechE, London, Paper 6, 1965*.
- [16] J. D. Lawson. Some criteria for a power producing thermonuclear reactor. *Technical report*, 1955.
- [17] D. D. Boetner M. J. Moran, H. N. Shapiro and M. B. Bailey. *Fundamentals of Engineering Thermodynamics 8th edition*. John Wiley and Sons, Inc., Hoboken, NJ, 2014.
- [18] R. Mitteau, B. Calcagno, P. Chappuis, R. Eaton, S. Gicquel, J. Chen, A. Labusov, A. Martin, M. Merola, R. Raffray, M. Ulrickson, and F. Zacchia. The design of the ITER first wall panels. *Fusion Engineering and Design*, 88(6–8):568 – 570, 2013. Proceedings of the 27th Symposium On Fusion Technology (SOFT-27); Liège, Belgium, September 24-28, 2012.
- [19] R. Mitteau, P. Stangeby, C. Lowry, and M. Merola. Heat loads and shape design of the ITER first wall. *Fusion Engineering and Design*, 85(10–12):2049 – 2053, 2010. Proceedings of the Ninth International Symposium on Fusion Nuclear Technology.
- [20] NASA. Binding energy curve - common isotopes. http://imagine.gsfc.nasa.gov/Images/teachers/posters/elements/booklet/energy_big.jpg.
- [21] A. R. Raffray and M. Merola. Overview of the design and R&D of the ITER blanket system. *Fusion Engineering and Design*, 87(5–6):769 – 776, 2012. Tenth International Symposium on Fusion Nuclear Technology (ISFNT-10).
- [22] Ch. L. Smith and S. Cowley. The path to fusion power. *PHILOSOPHICAL TRANSACTIONS OF THE ROYAL SOCIETY A-MATHEMATICAL PHYSICAL AND ENGINEERING SCIENCES*, 368:1091–1108, 2010.
- [23] R. Zanino, R. Bonifetto, F. Cau, A. Portone, and L. Savoldi Richard. CFD analysis of the ITER first wall 06 panel. Part I: Model set-up and flow distribution. *Fusion Engineering and Design*, 89(4):442 – 455, 2014.
- [24] R. Zanino, R. Bonifetto, F. Cau, A. Portone, and L. Savoldi Richard. CFD analysis of the ITER first wall 06 panel. Part II: Thermal-hydraulics. *Fusion Engineering and Design*, 89(4):431 – 441, 2014.